Drawing Number: 00035-LA03 Rev A

SNAP Mission Concept Omnibus Document

Drawn by:	A. Kim
Cognizant Engineer:	A. Kim
Date:	2003-10-07
Document Type:	SPEC
Category Code:	PS1000

Release History:

Rev	Description	Rev by	Check	Sys Engr	M.A.	C.M.	Date
A	Omnibus Mission Concept paper initial release	agk	mel			hdh	2003-10-07

SNAP Mission Concept

1. Introduction

In the past decade the study of cosmology has taken its first major steps as a precise empirical science, combining concepts and tools from astrophysics and particle physics. The most recent of these results have already brought surprises. The Universe's expansion is apparently accelerating rather than decelerating as expected due to the gravitational attraction of matter. This implies that the simplest model for the Universe — flat and dominated by matter — appears not to be true, and that our current fundamental physics understanding of particles, forces, and fields is likely to be incomplete.

The clearest evidence for this conclusion comes from the recent supernova measurements of changes in the Universe's expansion rate that directly show the acceleration. Figure 1 shows the results of Perlmutter et al. (1999) (see also Riess et al. (1998)) which compare the standardized brightnesses of 42 high-redshift Type Ia supernovae (SNe Ia) ($0.18 < z < 0.83$) with 18 low-redshift SNe Ia. The data implies that for a flat universe a fraction $\Omega_\Lambda = 0.72 \pm 0.08$ ($\Omega_M = 1 - \Omega_\Lambda$) of the critical density resides in a cosmological constant. More generally, this constrains the combination $0.8\,\Omega_M - 0.6\,\Omega_\Lambda$ to -0.2 ± 0.1, or a deceleration parameter $q_0 = -0.58$. These measurements indicate the presence of a new, unknown energy component that can cause acceleration, hence having an equation of state (ratio of pressure to energy density) with $w \equiv p/\rho < -1/3$.

This evidence for a cosmological constant or similarly negative-pressure vacuum energy ("dark energy") has received strong corroboration from combining cosmic microwave background (CMB) results (Balbi et al. 2000; Lange et al. 2001; Spergel et al. 2003), which are sensitive to the total energy density, with galaxy cluster measurements (Bahcall et al. 1999; Efstathiou et al. 2002; Percival et al. 2002), which probe the matter density Ω_M (see Figure 1). Two of these three independent measurements and standard inflation would have to be in error to make dark energy unnecessary in the cosmological model.

The dark energy might be the cosmological constant, with $w = -1$. Alternatively, it could be due to some other primordial field with different dynamical properties. The fundamental importance of a universal vacuum energy has sparked a flurry of activity in theoretical physics with several classes of models being proposed (e.g. quintessence (Ratra & Peebles 1988; Turner & White 1997; Caldwell, Dave, & Steinhardt 1998; Zlatev, Wang, & Steinhardt 1999), Pseudo-Nambu-Goldstone Boson (PNGB) models (Frieman et al. 1995; Coble, Dodelson, & Frieman 1997), cosmic defects (Vilenkin 1984; Vilenkin & Shellard 1994)). Placing some constraints on possible dark energy models, Perlmutter et al. (1999); Garnavich et al. (1998); Perlmutter, Turner, & White (1999) find that for a flat Universe, the data are consistent with a cosmological-constant equation of state with $0.2 \lesssim \Omega_M \lesssim 0.4$ (Figure 2), or generally $w < -0.6$ at 95% confidence level. Spergel et al. (2003) use WMAP CMB results in combination with other data to give the constraint $w < -0.78$. The cosmic string defect theory ($w = -1/3$) is already ruled out, domain walls ($w = -2/3$) are disfavored, and tracking quintessence models are disfavored.

To measure in detail the properties of the dark energy, more precisely and accurately, requires a new generation of experiments. The most well developed and understood method is the same one that led to the discovery of dark energy. Currently, in the Type Ia supernova technique the systematic and statistical errors are on the same order of magnitude: any new experiment to perform precision cosmology must eliminate or reduce the influence of all possible systematic uncertainties while discovering and measuring high-quality light curves and spectra of a statistically large number of supernovae.

In this paper, we describe the Supernova / Acceleration Probe (SNAP), designed as a dedicated mission to determine the values of the cosmological parameters and measure the properties and test possible models for the dark energy. In §2 we describe the data set necessary for performing precision cosmology with supernovae. This is based on the identification of systematic uncertainties that fundamentally limit the accuracy and on the number and redshift range of supernovae necessary to probe precisely the dark-energy parameters. The complementarity of weak gravitational lensing surveys in measuring cosmological parameters is discussed in §3. We present in §4 the observing strategies and instrumentation suite tailored to provide the data that satisfy both the statistical and systematic requirements for the supernova and lensing surveys. In §6 we discuss the general properties of the SNAP surveys and the science resources they will provide.

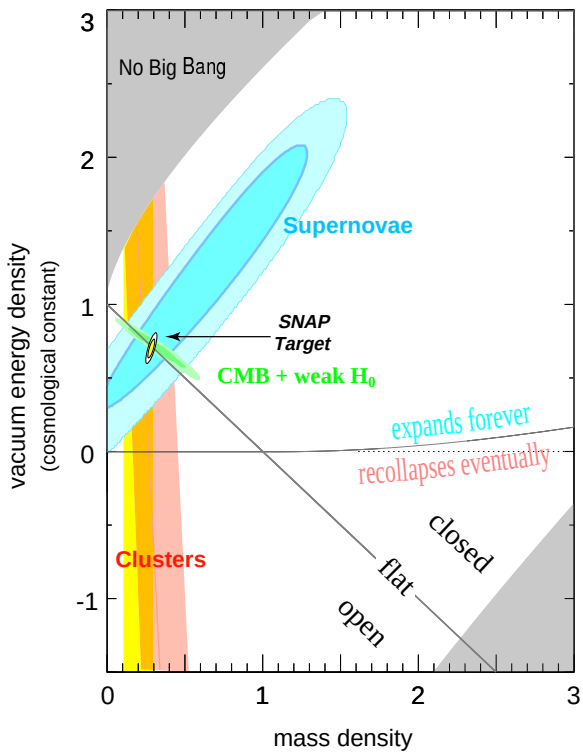

Fig. 1.— There is strong evidence for the existence of a cosmological vacuum energy density. Plotted are Ω_M—Ω_Λ confidence regions for SN (Perlmutter et al. 1999), galaxy cluster, and CMB data. These results rule out a simple flat, [$\Omega_M = 1$, $\Omega_\Lambda = 0$] cosmology. Their consistent overlap is a strong indicator for dark energy. Also shown is the expected confidence region from the SNAP satellite for an $\Omega_M = 0.28$ flat Universe.

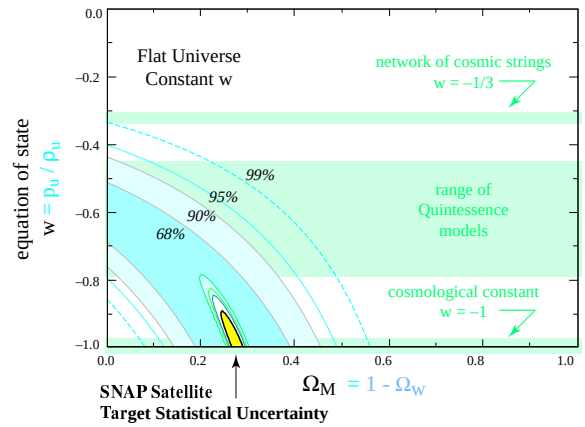

Fig. 2.— Best-fit 68%, 90%, 95%, and 99% confidence regions in the Ω_M–w plane for an additional energy density component, Ω_w, characterized by an equation-of-state $w = p/\rho$. (For Einstein's cosmological constant, Λ, $w = -1$.) The fit is constrained to a flat cosmology ($\Omega_M + \Omega_w = 1$). Also shown is the expected confidence region allowed by SNAP assuming $w = -1$ and $\Omega_M = 0.28$.

2. Supernova Cosmology Data Set

Our primary scientific objective is to use most efficiently the leverage available in the redshift-luminosity distance relationship to measure the matter and dark energy densities of the Universe with small statistical and systematic errors, and also test the properties and possible models for the dark energy. Type Ia SNe have already proved to be excellent distance indicators for probing the dynamics of the Universe. However, as we move toward the era of precision cosmology, we recognize that using the SNe for measuring cosmological parameters is fundamentally limited by potential systematic errors (as are all cosmological probes). The targeted data set must both address potential systematic errors and provide statistical errors that give the most leverage in the measurement of the dark-energy properties, especially the critical clue provided by the time variation of the equation of state. We proceed by listing the sources of systematic error, strategies to reduce their effects, and the fundamental limits in measuring cosmological parameters. We then determine which supernova observations give a comparable statistical error, which lead to requirements on the number of SNe we need to find, their distribution in redshift, and how precisely we need to determine each one's peak brightness.

2.1. Control of Systematic Uncertainties

2.1.1. Known Sources of Systematic Uncertainties

Below are identified effects which any experiment that wishes to make maximal use of the supernova technique will need to recognize and control. Following each item is the typical size of the effect on the SN brightness, along with a rough estimate of the expected *systematic* residual after statistical correction for such effects with the SNAP data set.

Extinction by Host-galaxy "normal" Dust: Cross-wavelength flux calibrated spectra will measure any

wavelength dependent absorption ($\sim$1–20% $\rightarrow$ 1%).

Gravitational Lensing by Clumped Mass: Inhomogeneities along the SN line of sight can gravitationally magnify or demagnify the SN flux. Since flux is conserved, the average of large numbers of SNe per redshift bin will give the correct average brightness. SNAP weak gravitational lensing measurements and micro-lensing studies can further help distinguish whether or not the matter is in compact objects ($\sim$1–10% $\rightarrow \sim 0.5$%).

K-Correction and Cross-Filter Calibration: Broadband photometry of supernovae at different redshifts is sensitive to differing supernova-frame spectral regions. K-corrections are used to put these differing photometry measurements onto a consistent supernova-frame passband. The current data set of time and light curve-width-dependent SN spectra needed for K-corrections is incomplete. Judicious choice of filter sets, spectral time series of representative SN Ia, and cross-wavelength relative flux calibration control this systematic ($\sim$ 0–10% $\rightarrow < 0.5$%).

Galactic Extinction: Supernova fields can be chosen toward the low extinction Galactic poles. Future SIRTF observations will allow an improved mapping between color excesses (e.g. of Galactic halo subdwarfs in the SNAP field) and Galactic extinction by dust ($\sim$1–10% $\rightarrow < 0.5$%).

Non-SN Ia Contamination: Observed supernovae must be positively identified as SN Ia. As some Type Ib and Ic SNe have spectra and brightnesses that otherwise mimic those of SNe Ia, a spectrum covering the defining rest frame Si II 6150Å feature for every SN at maximum will provide a pure sample ($\sim$10% $\rightarrow$ 0%).

Malmquist Bias: A flux-limited sample preferentially detects the intrinsically brighter members of any population of sources. Directly correcting this bias would rely on knowledge of the SN Ia luminosity function, which may change with lookback time. A detection threshold fainter than peak by at least five times the intrinsic SN Ia luminosity dispersion ensures sample completeness with respect to intrinsic SN brightness, eliminating this bias ($\sim$5–10% $\rightarrow$ 0%).

2.1.2. Possible Sources of Systematic Uncertainties

The following are sources of systematic error for which there is no direct evidence. However, a systematics-limited experiment must account for speculative but reasonable sources of error.

Extinction by Gray Dust

As opposed to normal dust, gray dust is postulated to produce wavelength independent absorption in optical bands (Aguirre 1999). Although physical gray dust grain models dim blue and red optical light equally, the near-IR light ($\sim$1.2 μm) is less affected. Cross-wavelength calibrated spectra extending to wavelength regions where "gray" dust is no longer gray will characterize the hypothetical large-grain dust's absorption properties. Armed with the extinction – color excess properties of the gray dust, broadband near-infrared colors can provide "gray" dust extinction corrections for SNe out to $z = 0.5$. The non-detection of forward-scattered X-ray halos around high-redshift quasars provide independent constraints on gray dust that is not in the form of needles. Recent upper limits are a factor of 10 below the density needed for the extinction to dominate the cosmological model behavior (Paerels et al. 2002). Moreover, the gray dust will re-emit absorbed starlight and thus contribute to the far-infrared background; current observations indicate that the FIR flux is attributable to point sources (Borys et al. 2002; Scott et al. 2002). Further observations of X-ray bright quasars through a range of redshifts and deeper SCUBA and SIRTF observations should further tighten the constraints on the amount of gray dust allowed.

Uncorrected Supernova Evolution

Supernova behavior itself may have systematic variations depending, for example, on properties of the progenitor systems. The distribution of these stellar properties is likely to change over time—"evolve"—in a given galaxy, and over a population of galaxies. Nearby SNe Ia drawn from a wide range of galactic environments already provide an observed evolutionary range of SNe Ia (Hamuy et al. 1996, 2000). The SN differences that have been identified in these data are well calibrated by the SN Ia light curve width-luminosity relation, leaving a 10% instrinsic dispersion. As of yet, there is no evidence for systematic residuals after correction, for example with galaxy type or supernova location (Sullivan et al. 2002). It is not clear whether any additional effects will be revealed with larger, more precise and systematic, low-redshift SN surveys (Aldering et al. 2003).

Theoretical models can identify observables that are expected to display heterogeneity. These key features, indicative of the underlying initial conditions

and physical mechanisms controlling the SN, will be measured with SNAP, allowing statistical correction for what would otherwise be a systematic error. The state of empirical understanding of these observables at the time SNAP flies will be explicitly tested by SNAP measurements. Presently, we perform Fisher matrix analysis on model spectra and light curves to estimate the statistical measurement requirements, and ensure that we have necessary sensitivity to use subsamples to test for residual systematics at better than the 2% level. This approach reveals the main effects of — as well as covariance between — the following observables:

Rise time from explosion to peak: This is an indicator of opacity, fused ^{56}Ni mass and possible differences in the ^{56}Ni distribution. A 0.1 day uncertainty corresponds to a 1% brightness constraint at peak (Höflich, Wheeler, & Thielemann 1998), and achieving such accuracy requires discovery within ∼2 days of explosion, on average, i.e. ∼30× fainter than peak. Current constraints on rise-time limit differences are two days (Aldering, Knop, & Nugent 2000).

Plateau level 45 days past peak: The light curve plateau level that begins ∼45 days past — and more than 10× fainter than — peak is an important indicator of the C/O ratio of the progenitor star, and fused ^{56}Ni. A 5% constraint on this plateau brightness corresponds to a 1% constraint on the peak brightness (Höflich, Wheeler, & Thielemann 1998). Current light curve measurements have not yet placed meaningful constraints on this ratio.

Overall light-curve timescale: The "stretch factor" that parameterizes the light-curve timescale is affected by almost all the aforementioned parameters since it tracks the SN Ia's light-curve development from early to late times. It is correlated with rise time and plateau level, and it ties SNAP's controls for systematics to the controls used in the current ground-based work. A 0.5% uncertainty in the stretch factor measurement corresponds to a ∼1% uncertainty at peak (Perlmutter et al. 1999). Stretch distributions are quite consistent between the current sets of low and high redshift supernovae (Perlmutter et al. 1999).

Spectral line velocities: The velocities of several spectral features throughout the UV and visible make an excellent diagnostic of the overall kinetic energy of SNe Ia. Velocities constrained to ∼250 km s^{-1} constrain the peak luminosity ∼1% (Höflich, Wheeler, & Thielemann 1998), given a typical SNe Ia expansion velocity of 15,000 km s^{-1}. Current data show smooth velocity development for a given supernova, but also clear differences between supernovae which have not yet been found to correlate with supernova luminosity (Branch & van den Bergh 1993).

UV spectral features: The positions of various spectral features in the restframe UV are strong metallicity indicators of the SNe Ia. By achieving a reasonable S/N on such features SNAP will be able to constrain the metallicity of the progenitor to 0.1 dex (Lentz et al. 2000). Spectral features in the restframe optical (Ca II H&K and Si II at 6150 Å) provide additional constraints on the opacity and luminosity of the SN Ia (Nugent et al. 1995). This spectral region has only recently begun to be explored with UV spectroscopy of nearby supernovae with HST.

Figures 3 and 4 show the particular light-curve and spectral parameters that can serve as indicators of supernova evolution. By measuring all of the above features for each SN we can tightly constrain the physical conditions of the explosion. This makes it possible to recognize subsets of SNe with matching initial conditions, ensuring a small luminosity range for each subset.

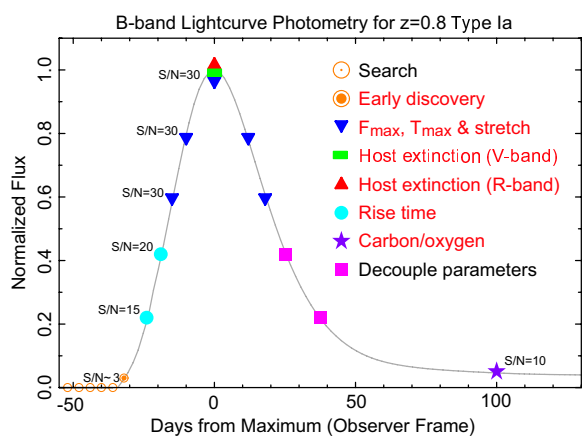

Fig. 3.— Sample B-band light curve for a $z = 0.8$ Type Ia supernova. Signal-to-noise targets are shown at different epochs for identification of possible systematic effects.

In addition to these features of the SNe themselves, we will also study the host galaxy of the supernova. We can measure the host galaxy luminosity, colors, morphology, and the location of the SN within the galaxy, even at redshifts z ∼1.7. The latter two observations are difficult or impossible from the ground.

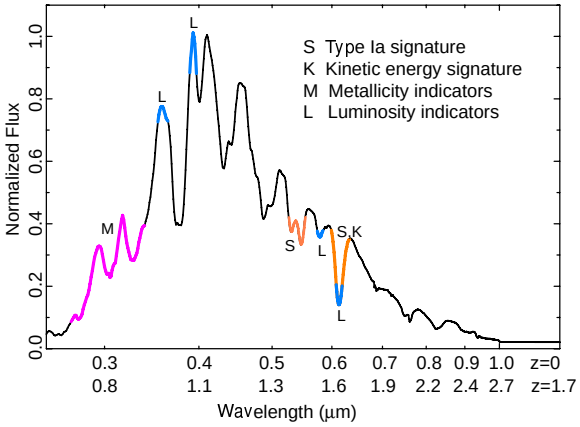

Fig. 4.— Type Ia spectra at maximum light showing line features associated with possible Type Ia supernova variation. The horizontal axis shows observer frame wavelengths for $z = 0$ and $z = 1.7$ supernovae.

2.2. Comparing Defined Subsets of Supernovae

The same subtyping strategy employed for evolution, based on observables tied to the explosion characteristics, can be more generally applied. The data (e.g., supernova risetime, early detection to eliminate Malmquist bias, light-curve peak-to-tail ratio, identification of the Type Ia-defining Si II spectral feature, separation of supernova light from host galaxy light, and identification of host galaxy morphology, etc.) make it possible to study each individual supernova and measure enough of its physical properties to recognize deviations from standard brightness subtypes. Only the change in brightness as a function of the parameters classifying a subtype is needed, not any intrinsic brightness. (Supernovae cannot change their brightness in one measured wavelength range without affecting brightness somewhere else in the spectral time series — an effect that is well-captured by expanding atmosphere computer models.)

The expected residual systematics from effects such as Malmquist bias, K-correction, etc. total ∼2%. Thus, a subset, or "like vs. like", analysis based on physical conditions should group SNe to within <2% in luminosity: this is in addition to a purely statistical correction for any second-parameter effects beyond the stretch factor.

As a precision experiment, SNAP is designed to distinguish between light-curve and spectral-parameter populations theoretically associated with subtle drifts not easily detected from the ground. By matching like to like among the supernova subtypes, we can construct independent Hubble diagrams for each, which when compared test systematic uncertainties down to the level of 1% in distance. Comparison within a redshift bin reveals possible systematics, while comparison over the redshift range within a subtype cleanly probes the cosmology.

2.3. Supernovae Sample to Probe the Dark Energy

The intrinsic peak-brightness dispersion of SNe Ia after light-curve shape and extinction correction is ∼10%, so from a statistical standpoint there is no need to measure the corrected peak brightness to better than ∼10%. With such statistical accuracy, a large sample, ∼2000 SNe Ia, is required to meet the measurement goals given in Table 1. This large sample is also necessary to allow model-independent checks for any residual systematics or refined standardization parameters, since the sample will have to be subdivided in a multidimensional parameter space of redshift, light curve-width, host properties, etc.

The importance of using SNe Ia over the full redshift range out to $z \sim 1.7$ for measuring the cosmological parameters is demonstrated in Figure 5, which shows the uncertainty in measuring the equation of state parameter, w, as a function of maximum redshift probed in distance surveys (Linder & Huterer 2002). This simulation considers 2000 SNe Ia measured in the range $0.1 \leq z \leq z_{\rm max}$, along with 300 low-redshift SNe Ia from the Nearby Supernova Factory (Aldering et al. 2003). A statistical error of 15% was assigned to each SN, which includes statistical measurement error and intrinsic error. A flat universe is assumed. Two classes of models were considered, one in which w is forced to be constant with time and a second in which we allow the possibility that w varies according to the linear expansion $w = w_0 + w'z$. The former case is applicable to a cosmological constant or a network of topological defects, while the latter case is applicable for almost all other models. Two types of experiments were considered. The first is an idealized experiment subject only to statistical errors, free of any systematic errors, and with extremely tight prior knowledge of the matter density. The second is a much more realistic model which assumes both statistical and systematic errors, with the systematic errors being very small like those SNAP can achieve. Shallower surveys are still assumed to somehow match SNAP's ca-

pabilities, with 2000 SNe and systematics bounded by $0.02(z/1.7)$ mag per redshift bin of width 0.1.

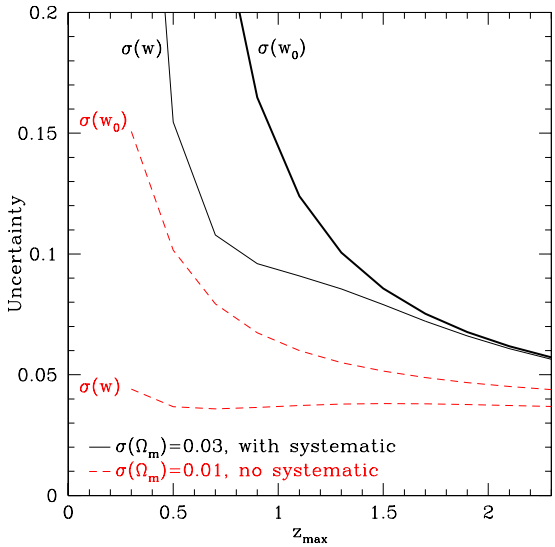

Fig. 5.— Accuracy in estimating the equation of state parameter, w, as a function of maximum redshift probed in distance surveys (Linder & Huterer 2002). The cases where w is assumed constant in time are labeled as $\sigma(w)$, while the cases where w is allowed to vary with time as $w = w_0 + w'z$ are labeled as $\sigma(w_0)$. The lower two curves assume that the experiment is free of any systematic errors, while the upper two curves are for the case where systematic errors are present at the 2% level. The top, heavy curve corresponds to the most realistic case. It is clear that even with modest systematic errors good accuracy requires probing to high redshift. In all cases a flat universe is assumed; a prior is also placed on Ω_M, with a less constrained prior of $\sigma_{\Omega_M} = 0.03$ for the cases where systematics are taken into account.

Even so, from this figure we conclude that a SNe Ia sample extending to redshifts of $z > 1.5$ is crucial for any realistic experiment in which some systematic uncertainties remain after all statistical corrections are applied. A similar redshift range requirement results for estimating w'. It is also clear that ignoring systematic errors can lead to claims which are too optimistic.

Although current data indicate that an accelerating dark energy density—perhaps the cosmological constant—has overtaken the decelerating mass density, they do not tell us the actual magnitude of either one. These two density values are two of the fundamental parameters that describe the constituents of our Universe and determine its geometry and destiny. SNAP is designed to obtain sufficient brightness-redshift data for a large enough range of redshifts ($0.1 < z < 1.7$) that these absolute densities can each be determined to unprecedented accuracy (see Figure 1). Taken together, the sum of these energy densities then provides a measurement of the curvature of the Universe, independent of the CMB, an important consistency check on the cosmological model.

Assuming that the dark energy is the cosmological constant, this experiment can simultaneously determine mass density Ω_M to accuracy of 0.02, cosmological constant energy density Ω_Λ to 0.04 and curvature $\Omega_k = 1 - \Omega_M - \Omega_\Lambda$ to 0.04. The expected parameter measurement precisions for this and other cosmological scenarios are summarized in Table 1; note that these values are sensitive to the specific choice of dark energy model and parameter priors — generally the cosmological constant scenario offers the *least* restrictive bounds.

The use of supernovae as standard candles is one of very few methods that can study the dark energy directly, and test alternative dark energy candidates. Assuming a flat Universe with a known prior mass density Ω_M and a dark energy component with a non-evolving equation of state, this experiment will be able to measure the equation of state ratio w with accuracy of 0.05 (for constant w), at least a factor of five better than the best planned cosmological probes, when realistic systematic uncertainties are included (Weller & Albrecht 2001, 2002). With such a strong constraint on w we will be able to differentiate between the cosmological constant and a range of dynamical scalar-field ("quintessence") particle-physics models (see Figure 2). Moreover, the supernova method is unique in its sensitivity to the time variation of the equation of state, w'. This quantity, generically predicted to be nonzero by high energy physics theories, provides a crucial clue to the underlying fundamental physics.

3. Cosmology with Weak-Lensing

The weak gravitational lensing of background galaxies by foreground dark matter (large-scale structure) provides a direct measurement of the amount and distribution of dark matter. In recent years many groups have measured the shape distortions of field

TABLE 1

SNAP 1-σ STATISTICAL AND SYSTEMATIC UNCERTAINTIES IN PARAMETER DETERMINATION

	σ_{Ω_M}		σ_{Ω_Λ} (or σ_{Ω_w})		σ_w		$\sigma_{w'}$	
	stat	total	stat	total	stat	total	stat	total
$w = -1$	0.01	0.02	0.04	0.04	···	···	···	···
$w = -1$, flat	···	···	0.01	0.01	···	···	···	···
$w = \mathrm{const}$, flat	···	···	0.02	0.02	0.06	0.08	···	···
flat; Ω_M known; $w = \mathrm{const}$	···	···	···	···	0.02	0.03	···	···
flat; Ω_M known; $w(z) = w_0 + w'z$	···	···	···	···	0.05	0.06	0.15	0.19

galaxies due to weak lensing and used these shear measurements to set constraints on cosmological parameters. The second moment of the shear field in a number of weak lensing surveys using ground and space-based data has provided a constraint on the mass power spectrum $\Omega_M \sigma_8^{0.5}$ that is comparable to the constraints set by more traditional methods such as the abundance of X-ray clusters. Current weak lensing surveys seeking to measure the higher order moments of the shear field and the magnification of background galaxies promise to provide an independent measure of Ω_M, thus breaking the degeneracy between Ω_M and σ_8. For a review of the techniques used to measure weak lensing and the current status of weak lensing measurements, see Refregier (2003).

Several conditions are necessary to make high signal-to-noise weak lensing measurements. A wide field-of-view is necessary to survey sufficient area so that the shapes of millions of background galaxies can be measured, and to overcome cosmic variance. Fine imaging resolution is necessary to measure the shapes of a high spatial density of background galaxies, and beat down shot noise on small scales. It is particularly important to be able to resolve many small, distant galaxies beyond a redshift of $z \gtrsim 1$. A stable point spread function (PSF) and a minimal level of internal optical distortions are essential for the precise measurement of galaxy shapes. Satisfying all of these requirements will inevitably require a wide-field space based imaging telescope in a thermally stable orbit.

Two major weak lensing applications are enabled by the SNAP mission. The first entails using weak lensing statistics to measure the mass power spectrum at high signal-to-noise in several redshift bins. Such measurements place constraints on cosmological parameters such as Ω_M and w. The second application is dark matter mapping and the unbiased detection of galaxy clusters by mass. The high surface density of resolved background galaxies enables the construction of both two- and three-dimensional maps of the foreground dark matter distribution. As well as providing further constraints upon cosmological parameters, these trace the growth of structure in the Universe and can be compared to the galaxy distribution in order to study the bias between mass and light.

3.1. Cosmological Parameters

Weak lensing measurements require a wide survey area to rapidly increase the total number of galaxies and to overcome cosmic variance. The size of the smallest resolved galaxies in a survey is driven by the size and stability of the telescope's PSF. With a high-throughput, space-based 2 meter telescope, an exposure time of 2000s will resolve significant numbers of galaxies in the scientifically interesting range beyond $z \gtrsim 1$. These can be successfully separated from low-z galaxies using photometric redshift estimates for which near-IR detectors are essential. This technique is inaccessible from the ground because convolution with the large and unstable PSF destroys the shape information needed in small and distant galaxies.

The broad redshift range of source galaxies enabled by space-based surveys provides a strong lever arm on the constraint of w. The increased space density of galaxies also enables the measurement of higher-order correlation functions of the shear field to break degeneracies between Ω_M and other cosmological parameters (Refregier et al. 2003). By measuring the shapes, sizes, and photometric redshifts of 100 million galaxies, tight constraints can be put on the dark mat-

ter power spectrum as well as the parameters Ω_M and w. These constraints are comparable to the constraints placed by the SN survey. However, these constraints are orthogonal to the constraints set by SNe and are thus a crucial element in the quest to understand dark matter and dark energy.

In Figure 6 we show the expected measurement of the matter power spectrum possible with 100 million galaxies over 300 square degrees divided into 2 redshift bins. The upper curve represents a measurement using resolved source galaxies with $z > 1$ and the lower curve represents $z < 1$ galaxies. In this manner, the evolution of the power spectrum is measured in a way not possible from the ground. In Figure 7 we show the joint constraints on Ω_M and w that we can draw using 10 million galaxies (deep survey); 100 million galaxies (wide survey); and 100 million galaxies divided into two redshift bins. Note that the constraints from weak lensing are largely orthogonal to the constraints from SNe. Thus, weak lensing complements the supernova technique in deriving constraints on w.

3.2. Dark Matter Mapping

Mass maps can be reconstructed from the observed shear field. These are sensitive to any mass along a given line of sight, regardless of its nature or state. The resolution of the maps depends on the size of the spatial element in which shear can be accurately measured. The SNAP lensing survey has been tailored to resolve the shapes of ≈ 100 galaxies per square arcminute. For source galaxies with an intrinsic ellipticity distribution $\sigma_\epsilon = 0.31$, (Rhodes, Refregier, & Groth 2000), this will achieve a signal-to-noise of unity in a 1 square arcminute cell, over 300 square degrees. The planned SNAP supernova survey will exceed even this density requirement by at least a factor of three (Massey et al. 2003). Thus, SNAP opens up a new regime of dark matter mapping allowing direct connections to be made between mass and light on fine scales over a very wide field of view. In Figures 8 and 9 we demonstrate the precision with which SNAP will be able to map the projected dark matter distribution. This will allow the relationship between mass and light to be examined to high accuracy over a large range of wavelengths.

Nine optical and near infrared filters spanning 0.35 – 1.7 μm, as envisioned for SNAP, would enable photometric redshifts to be calculated with an accuracy of $\delta z \lesssim 0.03$ (Massey et al. 2003). This is ideal

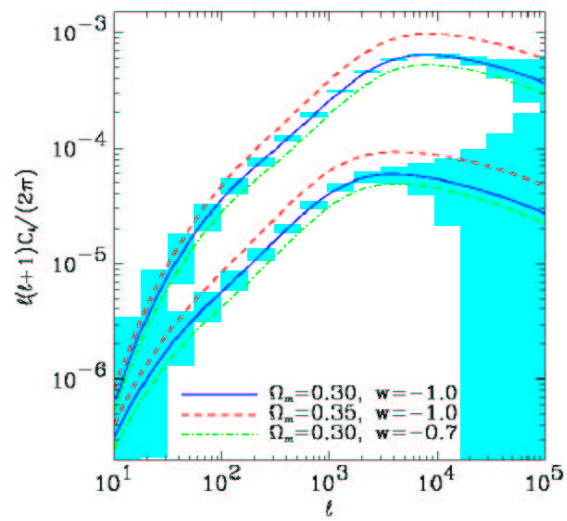

Fig. 6.— The dark matter power spectrum in two redshift intervals. The upper curve represents a measurement made with lens galaxies at $z > 1$ and the lower curve a measurement with $z < 1$. Three different cosmological models are shown and it is clear that the 100 million resolved galaxies in the SNAP wide survey will distinguish between cosmological models even after being divided into redshift intervals. Therefore, high signal-to-noise measurements of the evolution of the power spectrum will be possible.

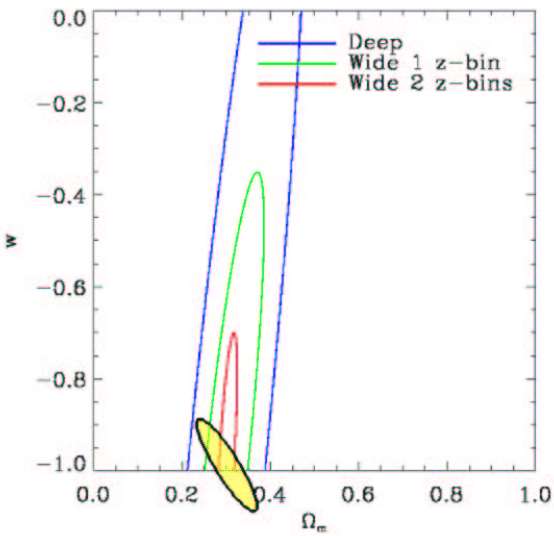

Fig. 7.— The joint constraints on Ω_M and w possible with the SNAP deep and wide surveys. After dividing the wide survey into two redshift intervals, the constraints are similar in size to the SN constraints (shown as a yellow ellipse). Since the weak lensing constraints are largely orthogonal to those of SN, weak lensing plays a crucial role in SNAP's ability to measure w.

for the making 2-dimensional mass maps in multiple redshift slices, and even fully 3-dimensional mass reconstructions. This redshift tomography is much less effective from the ground, because of the lower surface density of resolved galaxies, and cannot be extended as far. Space-based imaging is needed to resolve sufficient source galaxies at $z > 1$ and follow the growth of structure through a scientifically interesting range of structure evolution. Furthermore, high-resolution images coupled with photometric redshifts permit the use of a recently formulated approach to 3-D mapping (Taylor 2001) which recreates the full 3-D mass distribution by simultaneously considering both the shear estimator and the photometric redshift of a galaxy. Applied to the SNAP deep survey, this technique will detect mass overdensities with a 1σ sensitivity of $10^{13} M_{\odot}$ at $z = 0.25$.

3.2.1. Weak-Lensing Program

Part of the SNAP primary mission is a weak gravitational lensing survey. Lensing provides an independent and complementary measurement of the cosmological parameters through the mapping of galaxy shape distortions induced by mass inhomogeneities in the Universe. The strengths that make SNAP excellent for supernova observations apply to lensing as well; a wide-field imager in space with stable and narrow point-spread-functions can provide large survey areas, accurate shape measurements, and high galaxy surface densities. The SNAP supernova fields will serve as a deep lensing field while a second larger-solid-angle field specifically tailored for lensing will be observed to a shallower depth.

The weak lensing program calls for a five-month wide-field survey to observe the shapes and sizes of ~ 100 million galaxies which will complement the supernova survey. In this time, we obtain as much solid-angle as possible within the constraints of telemetry. The telemetry limits the number of images that can be sent to Earth and sets the exposure time of the observations. Cosmic-ray contamination is not so important given the large number of galaxy sources in the image; although each pointing will be dithered, further repeat observations of a field are unnecessary. Multi-filter data, particularly in the near-IR, are desired for accurate photometric redshift determination. The important observing parameters of this and the supernova programs are summarized in Table 2.

A full description of the SNAP weak lensing pro-

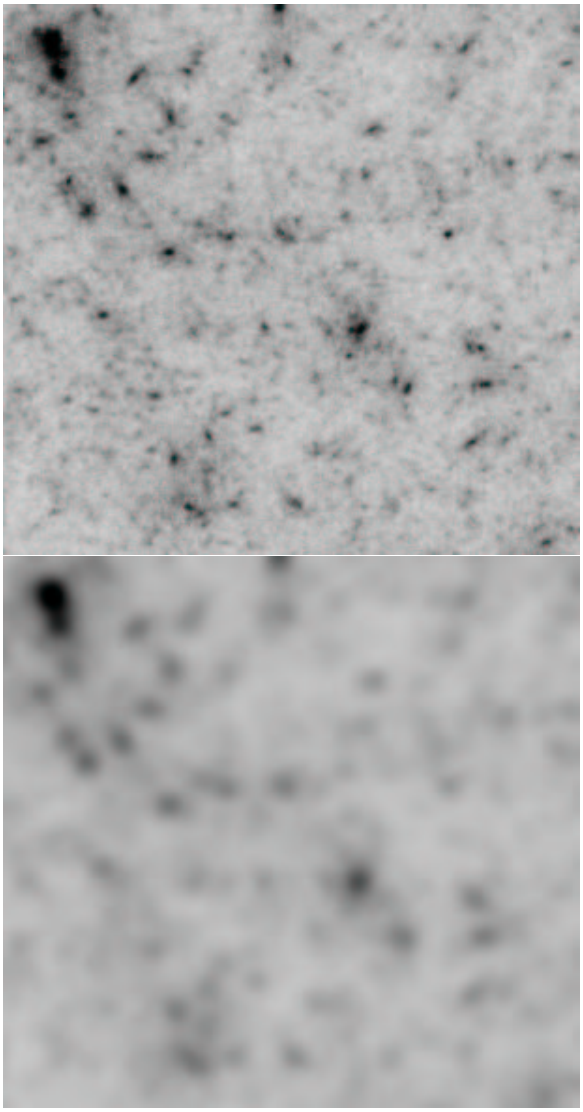

Fig. 8.— The first panel shows maps of mass, projected along a line of sight out to $z = 1$, in a CDM N-body simulation by (Jain, Seljak and White 2000). The field is 30'×30'. The second panel shows the same mass map smoothed on one arcminute scales.

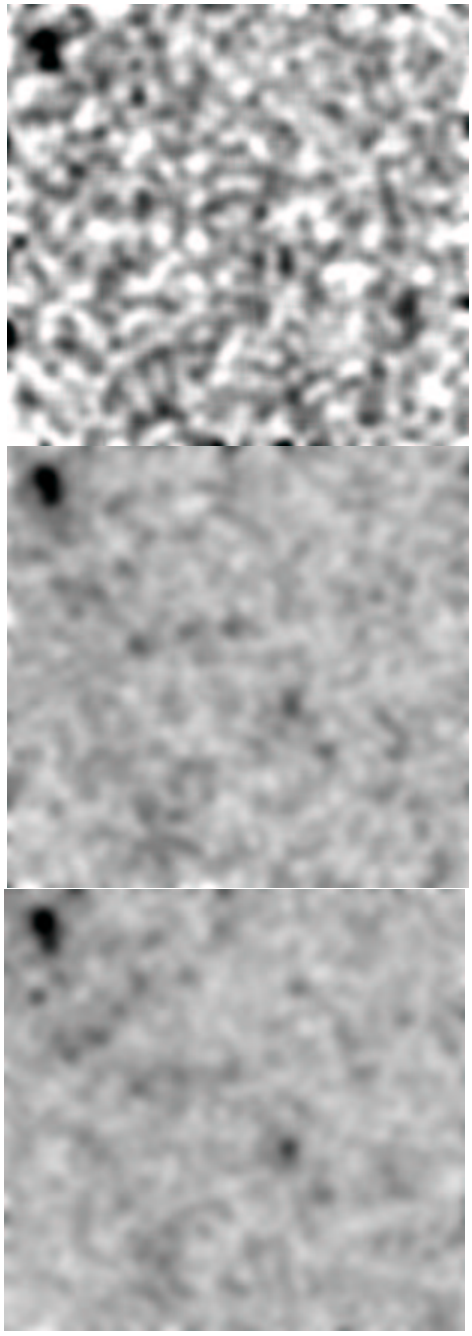

Fig. 9.— The three panels show the reconstructed mass maps that could be made from observations in a typical ground-based cosmic shear survey (top), the SNAP wide survey (100 gal per square arcminute) (center), and the SNAP deep survey (∼250 galaxies per square arcminute) (bottom). All are smoothed on 1' scales and the S/N of the map from the SNAP wide survey is approximately one per pixel. Notice the greatly improved reconstruction of even small overdensities from space.

gram can be found in a separate series of papers (Rhodes et al. 2003; Massey et al. 2003; Refregier et al. 2003).

4. Baseline SNAP Experiment

To accomplish a rigorous investigation of the cosmological model, discovery and study of a larger number and more distant SNe (or any probe) is by itself insufficient. As shown in §2.1, we must address each of the systematic concerns while making precise SN measurements, requiring a major leap forward in the measurement techniques. The requirements placed on the SNAP instrument derive directly from the science goals.

The primary requirement is to obtain the corrected peak brightness vs. redshift of at least 2000 Type Ia SNe out to a redshift of $z = 1.7$. Identification of Type Ia SNe requires the measurement of characteristic features in their spectra, taken near peak luminosity. Host-galaxy redshift is also determined spectroscopically. The corrected peak magnitudes are derived from supernova rest-frame optical light curves and spectra.

To meet the scientific requirements imposed by the program of measurements, SNAP has a large, 0.7 square degree instrumented field of view and an observation cadence of 4 days, commensurate with the timescale over which supernova light curves change. Discovery and photometric follow-up are automatically accomplished with the imager that repetitively scans a fixed 15 square degrees of sky. The imager's large field-of-view gives a significant multiplex advantage; each exposure contains > 20 active supernovae. Observations in multiple filters yield multi-color rest-frame optical light curves. A spectrometer optimized for SN spectra is allocated observation time for follow-up spectroscopy and template building. The telescope aperture is constrained by the photometric and spectroscopic S/N requirements and the focal plane must accommodate the large field of view.[1]

4.1. Observation Strategy and Baseline Data Package

The two primary SNAP science programs, the supernova and weak gravitational lensing surveys, have individually-designed observing schedules which are described here and summarized in Table 2.

4.1.1. Supernova Program

A simple, predetermined observing strategy repeatedly monitors regions of sky near the north and south ecliptic poles together covering 15 square degrees, discovering and following SNe Ia that explode in those regions. Every field will be visited every four days for 16 months, with sufficiently long exposures that almost all SNe Ia in the SNAP survey region will be discovered within a few restframe days of explosion. (SNe at much higher redshifts on average will be found slightly later in their light curve rise times although their prior history is in the data.) The periodic observation of fixed fields ensures that every SN at $z < 1.7$ will have its light curve followed for at least several months in the rest frame as it brightens and fades.

The zodiacal light will be the dominant source of background given SNAP's fields, orbit, and shielding of Earth-shine. Our primary science target fields are located near the north and south ecliptic poles where natural zodiacal light is near minimum. The cosmic-ray flux contamination of 4×10^{-4}/sec/pix for 10.5 μm pixels will make multiple measures necessary to eliminate significant contamination of the images.

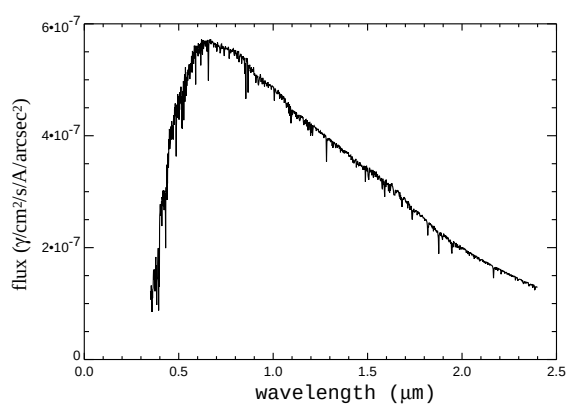

Fig. 10.— The zodiacal background will be the dominant source of background light for SNAP. Shown is the zodiacal photon flux toward the north ecliptic pole, the planned location for one of the SNAP supernova surveys.

Forty percent of the SNAP mission will be spent doing targeted spectroscopy of supernovae. Imaging

[1] The derived requirements for the SNAP instrument described here are preliminary and subject to change during the conceptual design phase.

[1] From http://crsp3.nrl.navy.mil/creme96/

TABLE 2
THE SNAP SURVEYS.

Program	Solid Angle per filter (sq. deg.)	Exposure per scan (s)	Cadence (days)	Visits
Supernova	7.5×2	Optical: 4×300 NIR: 8×300	4	120
Lensing	300	Optical: 4×500 NIR: 8×500	...	1

occurs simultaneously during these spectroscopic observations. The resulting images will cover random positions and orientations within the SNAP field and can be used to increase the depth of the survey and help with photometric and astrometric cross-calibration between detectors. However, these extra images are not further considered in this paper.

This prearranged observing program will provide a uniform, standardized, calibrated data set for each SN, allowing for the first time comprehensive comparisons across complete sets of SNe Ia. The following strategies and measurements will address, and often eliminate, the statistical and systematic uncertainties described in § 2.1.

- Blind, multiplexed searching.
- SNe Ia at $0.1 \leq z \leq 1.7$.
- Spectrum for every SN at maximum covering the rest frame Si II 6150Å feature and covering the UV.
- Spectral time series of representative SN Ia, with cross-wavelength relative flux calibration.
- A light curve sampled at frequent, standardized intervals that extends from ∼2-80 restframe days after explosion to obtain a light-curve-width- and extinction-corrected peak rest-frame B brightness to 10%.
- Multiple color measurements in 9 bands approximating rest-frame B at different redshifts.
- Final reference images and spectra to enable clean subtraction of host galaxy light.

The quality of these measurements is as important as the time and wavelength coverage, so we require control over S/N for these photometry and spectroscopy measurements to give high statistical significance for SNe over the entire range of redshifts. We also require control over calibration for these photometry and spectroscopy measurements, by collecting monitoring data to measure cross-instrument and cross-wavelength calibration.

Note that to date no single SN Ia has ever been observed with this complete set of measurements, either from the ground or in space, and only a handful have a data set that is comparably thorough. With the observing strategy described here, *every one* of ∼2000 followed SN Ia will have this complete set of measurements.

The requirements on spectroscopic exposure times and signal-to-noise are described in detail in Bernstein & Kim (2003). We adopt their prescribed exposure times; they find that a $z = 1.7$ supernova requires a 17 hours of integration with exposure times for supernovae at lower redshifts obeying a scaling factor of $(1+z)^6$.

SNAP will be unable to spectroscopically follow all of the highest redshift supernovae found in its survey. Kim et al. (2003) find that the precision of cosmological parameter measurements relies on having a significant number of high redshift supernovae, but their exact redshift distribution in unimportant. We adopt the distribution in Figure 11 for the spectroscopically confirmed supernovae.

4.1.2. Weak-Lensing Program

The strengths that make SNAP excellent for supernova observations apply to lensing as well; a wide-field imager in space with stable and narrow point-

spread-functions can provide large survey areas, accurate shape measurements, and high galaxy angular-surface densities. The SNAP supernova fields will thus serve as a deep lensing field.

The weak lensing program calls for a five-month wide-field survey to observe the ~ 100 million galaxies which will complement the supernova survey. In this time, we obtain as much solid-angle as possible within the constraints of telemetry. The telemetry limits the number of images that can be sent to Earth and sets the exposure time of the observations. Cosmic-ray contamination is not so important given the large number of galaxy sources in the image; although each pointing will be dithered, further repeat observations of a field are unnecessary. Multi-filter data, particularly in the NIR, are desired for accurate photometric-redshift determination. The important observing parameters of this and the supernova programs are summarized in Table 2.

A full description of the SNAP weak lensing program can be found in a separate series of papers (Rhodes et al. 2003; Massey et al. 2003; Refregier et al. 2003).

4.2. Mission Description

A high-Earth orbit is highly advantageous from the standpoint of achieving passive detector cooling. Our planned elliptical orbit has a geosynchronous period of three days, a $25R_\oplus$ apogee, and a $2.5R_\oplus$ perigee high enough to avoid the inner Van Allen belt whose energetic protons would otherwise seriously limit mission and detector lifetime.

Having the SNAP fields at the ecliptic poles places the sun at nearly right angles to our view direction throughout the year. In a high-Earth orbit, a low orbital inclination serves to keep the Earth and moon also nearly at right angles to our view direction. We utilize this viewing geometry in several ways. First, the solar panels can be rigidly body-mounted on the sunward side of the spacecraft, which avoids the cost, failure modes, and structural flexibility of deployed panels. Second, the passive cooling radiator can be rigidly located on the antisunward side of the spacecraft, in permanent shadow. Third, the stray light baffling can be optimized for a limited range of solar roll and elevation angles, and for a limited range of Earth elevation angles. We plan to have the spacecraft perform 90 degree roll maneuvers every 3 months during the mission, to keep up with the mean ecliptic longitude of the sun. The detector array has a 90 degree roll symmetry that allows its photometric data acquisition to continue from season to season.

4.3. Telescope

The requirements placed on the SNAP telescope derive directly from the science goals and the mission constraints. The wavelength coverage is determined by the need to measure a number of filter bands across the visible and NIR wavelength range, spanning roughly 0.35 μm to 1.7 μm, and to conduct low-resolution spectroscopy of each supernova near maximum light to extract features allowing detailed classification. This requirement effectively rules out refracting optical trains, and drives the telescope toward all-reflective optics. The light gathering power is set by the need to discover distant supernovae early in their expansion phases and to permit accurate photometry and low resolution spectroscopy near maximum light. This requirement can be met with a minimum aperture of about two meters. Image quality is also a factor in determining signal-to-noise ratio (S/N) because of the effects of natural zodiacal light and detector noise. For a two-meter aperture and one-micron wavelength, for example, the Airy disk size is 0.13" FWHM and we intend to achieve angular resolution near the diffraction limit at wavelengths longward of one micron. To match this diffraction spot size to the size of typical silicon pixels (~ 10 μm) one must adopt an effective focal length of about 20 meters. This same focal length is also a good match in the NIR where wavelengths up to 1.7 μm are to be observed using HgCdTe detectors whose pixels are 18–20 μm in size. Finally, a large field of view is needed for its multiplex advantage: a large number of sky pixels being observed in parallel contributes directly to the observing time per target for a given cadence and survey field size. Our science requirements are met if this field of view is the order of one square degree, of which about 0.7 square degree will be instrumented by detector pixels. The ratio of working field area to diffraction patch area is about 800 million, comparable to the total number of detector pixels. By means of dithering we expect to recover photometric measurements good to a few percent accuracy. Undersampling, dithering, cosmic ray hits, and many other effects are included in the exposure time calculator developed by Bernstein (2002).

The image quality of the telescope is driven in part by the S/N requirement, and also by the potential systematic supernova spectrum contamination by un-

wanted light from the supernova host galaxy. We have presently baselined a system Strehl ratio of 0.90 at one micron wavelength, corresponding to an RMS wavefront error (WFE) of 50 nm, or a Strehl ratio of 0.77 at the commonly used test wavelength of 0.633 μm.

4.3.1. Optical Configuration

Prospective launch vehicles (Delta IV, ATLAS V, SeaLaunch) and payload fairing dimensions impose limits on the overall telescope size and its mass. An overall payload length of about the SNAP observatory. Through a series of packaging exercises we have explored ways to fit the maximum length stray light baffle into available launch fairings, and find that with a short optical package, ~ 3 m in length, and a tall outer baffle, the required stray light rejection can be achieved.

To accommodate dimensional limitations and wide-field optical quality, the three mirror anastigmat described by Korsch (1977) is used. A schematic view is shown in Figure 12.

Details of the SNAP optical configuration have been determined by an iterative process involving exploring various alternative choices for focal length, working field coverage, and packaging constraints (Lampton 2002). The optimized optical parameters are summarized in Table 3. The overall length of the optical train is 3.3 meters. Compared with the 21.66 meter effective focal length, this system has an effective telephoto advantage of about 6.5. The mirrors are pure conic sections of revolution having no polynomial terms. The use of higher polynomial terms has not yet been explored. The location of the vertex of each element is listed in a Cartesian (X,Z) coordinate system whose origin is the vertex of the primary mirror.

4.3.2. Mechanical Configuration

The launch environment imposes both stiffness and strength requirements on the payload. Vehicle aeroelastic stability concerns prescribe the needed payload stiffness in terms of minimum structural frequencies in the axial (~ 25 Hz) and lateral (~ 10 Hz) directions. The launch environment includes both quasi-steady and random acceleration events that are combined to establish the peak loads, or strength requirements for the payload. Preliminary estimates indicate the design loads will be the order of 12 G's axial and 8 G's in the lateral directions. The thermal environment will be 0°-40°C pre-launch, while the operational temperatures for the optical elements and structure will be actively controlled as dictated by the optics dimensional stability and instrument requirements.

For a space mission it is vital to create a mechanical configuration that provides an extremely stable metering structure that maintains the optical element alignment during ground testing, launch, and orbit operations. The concept adopted for SNAP is to create three structural components that will be brought together during spacecraft/payload integration: a stiff low-precision outer baffle cylinder carrying the exterior solar panels and extensive thermal insulation; a stiff low-precision spacecraft bus structure that carries antennas, batteries, and other major spacecraft support components; and a stiff high-precision telescope structure comprising carbon-fiber metering elements, the kinematically-mounted mirrors, the instrumentation suite, and its own thermal control system. Figure 13 shows the overall payload and spacecraft layout, while Figure 14 shows details of the secondary and tertiary metering structures.

4.3.3. Materials

Space-proven optical mirror technology is largely based on two approaches: open-back Schott Zerodur glass ceramic composite material and Corning ultra-low expansion ULE glass honeycomb structure. For SNAP either technology has sufficiently low coefficient of thermal expansion and sufficiently well proven manufacturing techniques. Studies are underway exploring the detailed fabrication and test flows using either process.

The metering structure will utilize a low-CTE carbon-fiber construction. In particular, the secondary support tripod will have to maintain the primary to secondary spacing accurate to a few microns. This tripod and the other major metering components will certainly require a dedicated active thermal control system. We anticipate the need for five-axis motorized adjustment for the secondary mirror during ground integration, on-orbit observatory commissioning, and occasionally during science operations. For this reason we plan to include a hexapod or other multi-axis positioner into the secondary support structure.

The single highest priority bearing on the choice of mirror coating is the system throughput at the longest wavelengths where supernovae are the most distant and photons are the most precious. A secondary consideration is to establish a low thermal emissivity for

TABLE 3
OPTICAL SURFACES AND LOCATIONS

Optic	Diameter (m)	Central hole (m)	Curvature (m^{-1})	Asphericity	X location, (m)	Z location (m)
Primary	2.00	0.5	-0.2037466	-0.981128	0	0
Secondary	0.45	none	-0.9099607	-1.847493	0	-2.00
Folding flat	0.66 × 0.45	0.19 × 0.12	0	0	0	0.91
Tertiary	0.68	none	-0.7112388	-0.599000	-0.87	0.91
Focal plane	0.567	0.258	0	0	0.9	0.91

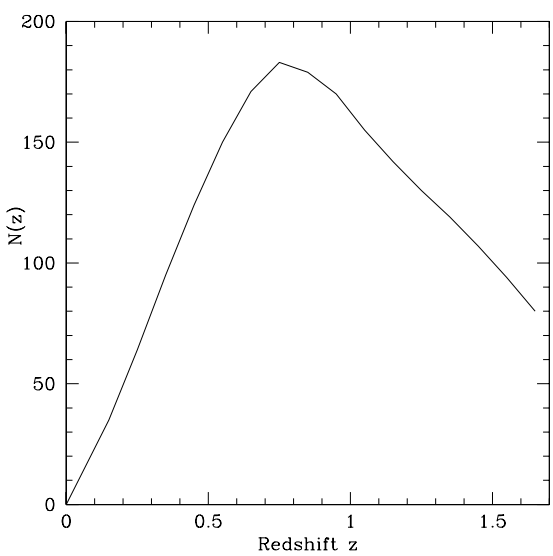

Fig. 11.— Due to time constraints, SNAP will spectroscopically follow a subset of the highest redshift supernovae found in its survey.

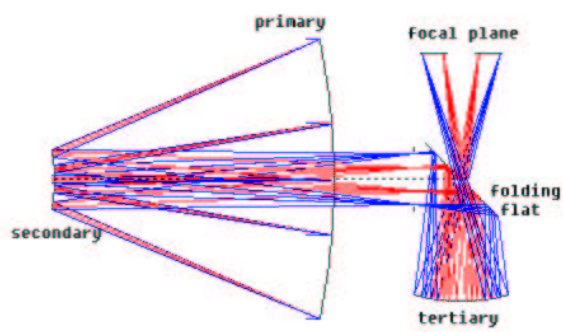

Fig. 12.— SNAP optics layout. The entrance pupil is defined by the primary mirror. A field stop is located behind the primary mirror (vertical marks) for stray light control. The exit pupil is at the folding mirror.

the mirrors so that operating them at a reasonable temperature, approx 290K, will not seriously impair our astronomical sensitivity in the near IR bands. The most common coating for astronomical mirrors at visible wavelengths is SiO overcoated aluminum. It offers outstanding durability and unmatched reflectance throughout the visible band, 0.4 to 0.7 microns. A less common choice is protected silver, which is less efficient in the blue but more efficient in the red and near IR. Our SNAP optical system needs to operate over a wavelength range extending to 1.7 microns in the near IR, and has four reflections. The throughput therefore varies as the fourth power of the mirror coating reflectivity. We have baselined the use of protected silver rather than protected aluminum owing to its higher reflectance in the near infrared.

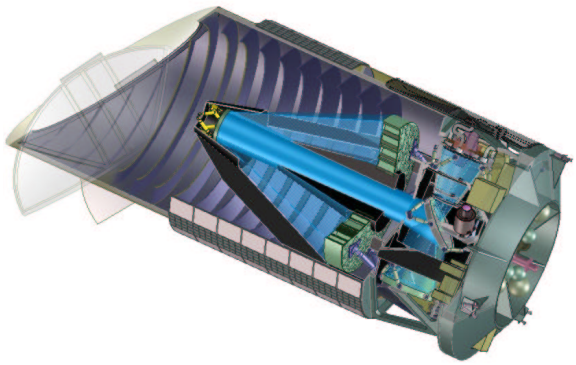

Fig. 13.— Cutaway view of SNAP. The entire telescope telescope attaches to the spacecraft structure at right by means of bipods. The outer baffle, shown cut away, also attaches to the spacecraft structure by means of its separate supporting struts. A hinged split door, shown open in light gray, protects the cleanness of the optics until on-orbit commissioning begins. Solar panels are fixed, not deployed.

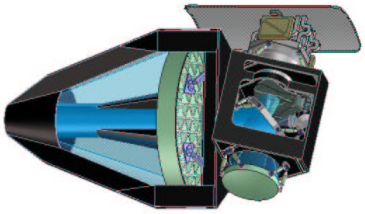

Fig. 14.— Telescope metering structure (carbon fiber, shown in dark gray) provides precision control of optical element spacings and orientations. Forward of the primary mirror, the secondary is supported on adjusters within the secondary baffle. Aft of the primary mirror, the tertiary metering structure supports the folding flat, the tertiary, and the focal plane instrumentation. The passive radiator at top is thermally but not structurally linked to the focal plane instrumentation.

4.3.4. Geometric-Optics Performance

The optical performance of our baseline optical telescope is fundamentally limited by aberrations and manufacturing errors at short wavelengths, and by diffraction at long wavelengths. Accordingly, our expected performance figures divide into two areas: the geometrical ray traces that quantify the aberrations and the pupil diffraction studies. We summarize the key performance items in Table 4 and Figure 15 below.

From spot diagrams at various off axis angles, we have compiled the statistics on the mean radial centroid of ray hits in the focal plane, and the second moments of the spot distributions. These are listed in the Table 5 in the form of the two orthogonal RMS breadths (radial RMS and tangential RMS) in columns 3 and 4. Combining these by their root-sum-square gives a two-dimensional measure of the spot size, listed in column 5 below as a linear focal plane dimension, and as an angular size on the sky in milliarcseconds in column 6. At the inner and outer radii of the image annulus, the FWHM becomes as large as 60 milliarcsec, although in the midrange of the annulus it is smaller.

Distortion is another fundamental optical aberration, but unlike the other Seidel aberrations distortion does not impact the S/N nor does it directly impact the detection of supernovae. It does however cause the loci of scanned field objects to depart from parallel tracks in the focal plane, and does complicate the weak lensing science. In our baseline design, we have disregarded distortion as a driver, in order to use all available design variables to maximize the working field of view and minimize the net geometrical blur. It is nonetheless important to explore the resulting distortion quantitatively. The TMA distortion is axisymmetric owing to the symmetry of the unfolded (powered) optical train, and in polar coordinates any off-axis angle maps onto a single focal plane radius independent of azimuth angle. The distortion is therefore purely radial. Table 5 lists the radial distance of an off axis field point as a function of the sine of the off axis angle, and the departure from proportionality to the sine of that angle. From Table 5 it is seen that the TMA distortion is of the pincushion type, having increased magnification toward the extremity of the field. Compared to a linear mapping of $\sin\theta$ onto focal plane radius, the distortion amounts to about two percent.

TABLE 4

OPTICAL PERFORMANCE SUMMARY

Parameter	Value/Performance
Focal Length	21.66 meters
Aperture	2.0 meters
Final focal ratio	f/10.83
Field	Annular, 6 to 13 mrad; 1.37 sq deg
RMS geometric blur	2.8 microns, average 1 dimension
Central obstruction	16% area when fully baffled
Vane obstruction	4% area, tripod

TABLE 5

OFF AXIS ANGLE, IMAGE MOMENT, AND RADIAL DISTORTION

OffAxis $\sin\theta$	Rfinal, (μm)	radial RMS, (μm)	tangential RMS (μm)	Total RMS (μm)	Total RMS (milliarcsec)	LinModel	Diff (μm)
0.006	129122	3.32	1.60	3.69	34.88	129960	-838
0.007	150838	3.33	1.60	3.69	34.97	151620	-782
0.008	172649	3.18	1.59	3.56	33.65	173280	-630
0.009	194565	2.83	1.51	3.21	30.36	194940	-373
0.010	216600	2.28	1.37	2.66	25.17	216600	0
0.011	238769	1.57	1.35	2.07	19.60	238260	509
0.012	261086	1.18	1.89	2.23	21.09	259920	1165
0.013	283565	2.09	3.23	3.85	36.41	259920	1983
			AVERAGE=	3.12	29.52		

4.3.5. *Pupil Diffraction*

For a star at infinity and a telescope focused at infinity, the pupil diffraction pattern is computed using the Fraunhofer formalism, and the focal plane irradiance is simply the square of the modulus of the two-dimensional Fourier transform of the pupil. For quantitative studies of our expected point spread function and our diffracted light background, we have computed this irradiance function for a variety of prospective pupils. Figure 16 below shows this irradiance in a two-dimensional logarithmic format. The vertical scale shows the extent of five orders of magnitude of irradiance. The pupil, shown at the right, has a two meter aperture, three tripod legs of 50mm width, and a central obstruction 0.8m in diameter. The assumed wavelength is 1.0 μm. The six spikes and the central Airy disk patterns are evident.

4.3.6. *Stray Light*

A comprehensive stray light control plan has been developed for SNAP. Our goal is to keep all stray light sources far below the natural zodiacal irradiance level as seen at the focal plane. The primary concern is of course sunlight scattered past the forward edge of the outer light baffle. This will require a minimum of two successive forward edges, since the light diffracted past a single edge would exceed the allowable irradiance at the primary mirror, assuming typical mirror scattering values. Another concern, during portions of the orbit where the fully illuminated Earth is seen, is scattered Earth light. When fully illuminated, the Earth stands opposite to the sun and the tall interior side of the outer baffle tube receives Earthshine. We have devised a baffle angle strategy that will help minimize sunlight and Earthshine seen at the primary mirror (see Figure 17 below). The blades are angled downward, so that even at the lowest Earth elevation, Earthshine reaches only their upper surfaces, while the primary mirror can see only their dark lower surfaces. In this way, a minimum of two scatters is needed for Earth light to reach the primary. Additional stray light occurs from the moon, stars, etc, and is being quantitatively tracked as our design process continues.

4.3.7. *Tolerances*

The departure of any surface from its nominal mathematical conic section, or the misplacement or misorientation of any of the surfaces, causes a wavefront error and a degraded image quality. One mea-

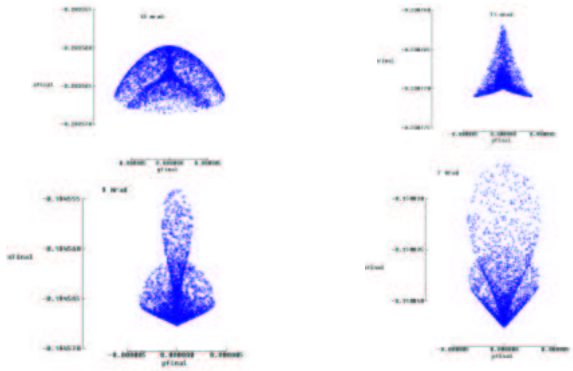

Fig. 15.— Ray trace spot diagrams. Upper left: 13 mrad off axis; upper right 11 mrad; lower left 9 mrad; lower right 7 mrad. Tick marks are spaced 5 μm in the focal plane.

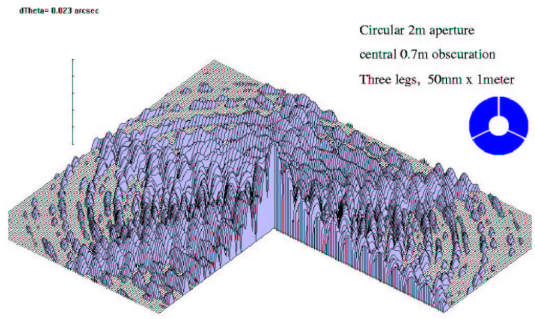

Fig. 16.— Focal plane irradiance defined by diffraction of a monochromatic incoming plane wave, 1.0 μm wavelength, through the pupil shown at right. Vertical scale (upper left) shows logarithmic five decade range of irradiance. Horizontal span is 5" $\times$ 5 " with steps of 0.023 arcsecond per image slice. The threefold symmetry of the pupil causes the six diffraction spikes evident in the figure.

Fig. 17.— Schematic treatment of the outer baffle interior vane arrangement. Sunlight is incident from the left, where the height of the baffle and its angled forward edge maintains the baffle interior in darkness. Earthshine is at times incident from the right, however, and therefore the vane angles require particular attention so that the lower vane surfaces are not illuminated by the Earth.

sure of this degradation is the telescope's Strehl ratio, which is the peak monochromatic image irradiance divided by the theoretical peak irradiance for the ideal diffraction limited image. The Strehl ratio can be converted into RMS wavefront error (RMS WFE) through Marechal's relation. To achieve a system Strehl ratio of 0.77 at 0.633 μm wavelength, the total WFE must not exceed 50 nm RMS. This allowed WFE will be apportioned into individual contributions as part of the detailed telescope design.

A tolerance budget has been developed based on a group of exploratory studies of the sensitivity of the geometrical spot size to variations in element curvatures, shapes, locations, and orientations. These calculations shows that by far the single most critical parameters are the primary mirror curvature and the spacing between primary and secondary mirrors, expected given the fast ($f/1.2$) primary mirror. A two-micron displacement of the secondary piston, or a two-micron displacement in the virtual image created by the primary mirror, is found to increase the RMS geometrical blur by about 3 μm. Similarly, a 15-micron lateral displacement or a 15-microradian tilt of the secondary mirror causes a 3-micron growth in the RMS geometrical blur.

The baseline SNAP telescope includes on-orbit mechanical adjustments that permit the relocation and reorientation of the secondary mirror, and possibly the tertiary mirror as well, to optimize image quality. By means of these adjustments we anticipate accommodating small shifts in any of the optical elements locations and orientations, allowing for correction of geometrical blur.

4.4. Imager

The wide field of view of the SNAP imager allows simultaneous batch discovery and photometry, and over the mission lifetime will yield $>$2000 SNe with the proposed photometric accuracy. More distant, less precisely measured SNe will also be available in our data set. Figure 3 shows critical points on the light curve and the desired measurement accuracy that the SNAP imager must furnish. We note that the stated signal-to- noise ratio (S/N) need not be achieved with a single measurement but can be synthesized from multiple measurements, taking advantage of the substantial time dilation for high-redshift SNe.

The SNAP imager addresses the above requirements using two detector technologies to efficiently

cover the wavelength range of 350 nm to 1700 nm. The visible region (350 nm to 1000 nm) is measured with Lawrence Berkeley National Laboratory CCD's new-technology n-type high-resistivity CCD's (Holland et al. 1999; Stover et al. 2000; Groom et al. 2000) which have high (∼80%) quantum efficiency for wavelengths between 0.35 and 1.0 μm. Extensive radiation testing shows that these CCD's will suffer little or no performance degradation over the lifetime of SNAP. A pixel size of 10.5 μm has been matched to the telescope diffraction limit at 1000 nm of 0.1 arcsec.

The NIR range (900 nm to 1700 nm) is measured with commercially available HgCdTe arrays. Current large area (2048 × 2048 pixel) HgCdTe detector devices have a pixel sizes in the range of 18 - 20 μm. The telescope optics are designed to give an angular pixel size of 0.17 arcsec, a good match to the telescope diffraction limit at 1700 nm. The SNAP baseline performance specifications require low read noise and dark current (< 5 e$^-$ for single read and $<$ 0.1 e$^-$/sec/pix, respectively), high quantum efficiency (>60%), and uniform pixel response. Imager detector specifications are given in Table 6. The evolution of the SNAP focal-plane design is described in Bebek et al. (2003).

The minimum filter set required is primarily determined by the precision needed for the K-correction, the reconstruction of the restframe B-band light from a set of laboratory-frame filter measurements. Six visible filters and three NIR filters are sufficient if they are derived from a B-band filter with logarithmic $(1 + z)$ scaling of their wavelength centers and widths. Figure 18 shows an array of visible and NIR filters. The set that we consider here consists of nine Johnson B filters logarithmically distributed in wavelength with effective wavelengths at 4400×1.15^nÅ for $n \in \{0, 1, ..., 8\}$. To enhance the amount of NIR light that is integrated, the individual NIR filters have twice the area of the individual visible filters.

The constraint that the satellite be rotated in 90° increments requires the filter pattern to remain symmetric with respect to two orthogonal axes. Consider the filter arrays in Figure 19. Note that the arrays can be scanned though an observation field left-to-right, right-to-left, top-to-bottom, and bottom-to-top, and that a given star will be measured with each filter bandpass but not necessarily the same physical filter. Note that any 90° rotation of the filter array can still measure the star field in all filter types.

As shown in Figure 18, underlying each NIR filter

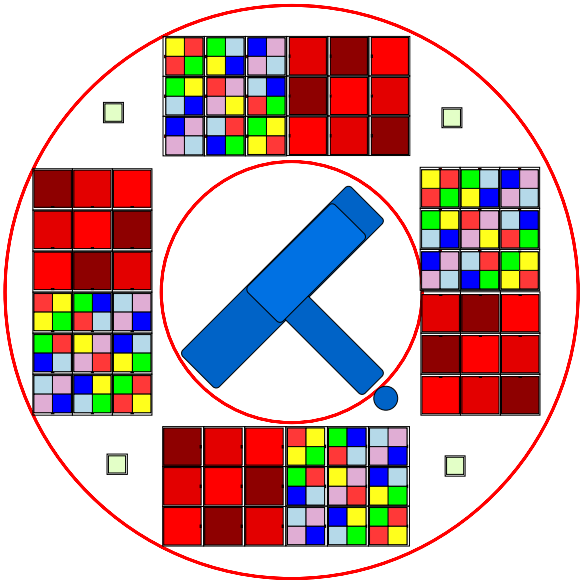

Fig. 18.— The SNAP focal plane working concept. The two axis symmetry of the imager filters allows any 90° rotation to scan a fixed strip of the sky and measure all objects in all nine filter types. The imager covers 0.7 square degrees. Underlying the filters, there are 36 2k x 2k HgCdTe NIR devices and 36 3.5k x 3.5k CCD's on a 140K cooled focal plane. The central rectangle and solid circle are the spectrograph body and its light access port, respectively. The spectrum of a supernova is taken by placing the star in the spectrograph port by steering the satellite. The four small, isolated squares are the star guider CCD's. The inner and outer radii are 129 and 284 mm, respectively.

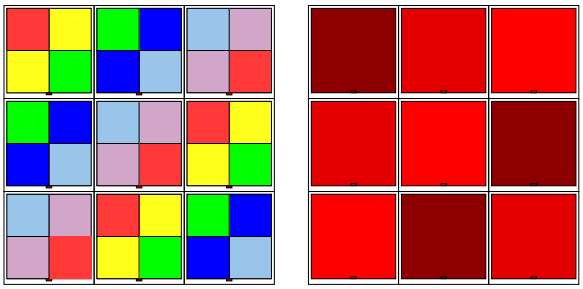

Fig. 19.— On the left is a two axis symmetric deployment of six filters types for the visible imager such that vertical or horizontal scans of the array through an observation field will measure all objects in all filters. On the right is the same concept for an array of three filter types for the NIR imager. The false colors indicate filters with the same bandpass.

TABLE 6
MISSION REFERENCE SPECIFICATIONS FOR THE IMAGER AND ITS SENSORS

Parameter	Visible	NIR
Field of View (deg^2)	0.34	0.34
Plate scale (arcsec)	0.10	0.17
Wavelength (nm)	350–1000	900 – 1700
$\langle$Quantum efficiency$\rangle$ (%)	80	60
Read noise (multiple reads) (e^-)	4	5
Dark current (e^-/s/pixel)	0.002	0.02
Diffusion (μm)	4	5
Number of filters	6	3

is one 2k $\times$ 2k, 18 μm HgCdTe device, 36 in total. Underlying each 2×2 array of visible filters is one 3.5k $\times$ 3.5k, 10.5 μm CCD, with 36 devices in all. The total number of pixels is $\sim$600 million.

The SNAP focal plane would be passively cooled to operate at 140K. Short flex cables penetrate the focal plane to bring the signals to the electronics located on the backside. The present conceptual design envisions an ASIC-based readout that would also operate at 140K; this avoids routing low-level analog signals long distances and reduces the size of the cable plant between the cold focal plane and the warm data acquisition electronics located to the side. Multi-band exposures of a point of sky will be achieved by shift-and-stare observations in which the pointings are shifted by the 2.9 arcmin width of the optical filters. Each pointing will consist of four 300-second exposures; the multiple exposures are for cosmic-ray rejection and dithering of our undersampled pixels. Within a scan, over one hundred pointings are required to cover the 7.5 square degrees in all filters to the desired depth. A scan of the north (south) field will be repeated every four days for 16 months for a total 120 scans.

4.5. Spectrograph

The spectrometer is used to make a positive identification of Type Ia SNe by observing the characteristic SiII feature at 6150 Å, measure the features associated with supernova heterogeneity, determine the redshift of the underlying host galaxies, build a template spectral library of SNe Ia, and link standard stars with the SNAP photometric system.

The silicon feature, with other features in the spectrum of a typical Type Ia SNe, shown in Figure 4, will allow a detailed characterization of parameters such as metallicity and ejecta velocities. The feature characteristics (position, width, height, etc.) are directly related to the peak magnitude through physical parameters such as temperature, velocity and progenitor metallicity. In models, the strongest sensitivity to the metallicity in the progenitor system lies in the rest-frame UV band, which defines a broad wavelength range, 0.4 - 1.7 μm, that must be covered by the instrument.

Of particular interest is the velocity and thermal broadening of all lines, which indicates that high-resolution spectroscopy is not required. The specific signature of Type Ia supernovae is the SiII line at $\lambda = 6150$Å (rest frame). This line is very broad (~ 200Å rest frame) and is broadened further by the redshift factor $(1+z)$ and shifted to $\sim 1.7\mu$m for $z = 1.7$. Other types of SNe, such as II or Ib, have lines of H or He in the same wavelength range, allowing the classification of all possible candidates. The broad features of the SN spectra and the non-negligible detector noise contribution for the faintest objects make a low-resolution spectrograph optimal: studies (Bernstein & Kim 2003) find an optimal resolving power $\lambda/\delta\lambda \sim 100$ at FWHM and 1 pixel per FWHM sampling, with constant resolving power in the 0.6-1.7μm range.

The field of view must include the underlying galaxy in order to determine its spectrum during the same exposure. This is necessary for subtraction of the host spectrum from the spectrum in the supernovae region, and for an accurate determination of supernova redshift. Based on the mean size of galaxies at red-

shift 1-2, a 3" × 3" field of view is sufficient. The main spectrograph specifications are summarized in Table 7.

4.5.1. *Instrument Concept Tradeoff*

The requirement for simultaneous acquisition of SN and host spectra, spectrophotometry for calibration purposes, and the high object acquisition precision that would be needed for a traditional long slit spectrograph, make a 3D spectrograph an attractive option. A 3D spectrograph reconstructs the data cube consisting of the two spatial directions X and Y plus the wavelength direction as shown in Figure 20. For each spatial pixel, the spectrum is reconstructed. Thanks to the 3" × 3" field of view, the pointing requirements are relaxed and the galaxy and SN data are acquired at the same time. Two principal techniques are indicated for 3D spectroscopy: first, the use of a Fourier Transform Spectrometer (FTS), and second, the use of integral field spectroscopy.

The FTS technique is based on the classical Michelson interferometer principle. When one of two flat mirrors is moved, the Fourier transform space of the wavelength is scanned. FTS is best applied at longer wavelengths, in a smaller wavelength range and higher spectral resolution than SNAP needs. The main drawback to an FTS on SNAP would be the need for a translating device with a quarter-millimeter throw and a positioning accuracy of a few nanometers. This would call for a complex mechanism, and for a very precise metrology system.

Integral field spectroscopy using traditional dispersers is based on one of the three generic techniques illustrated in Figure 21. Our trade studies indicate that the image slicer technique is preferred for SNAP. This

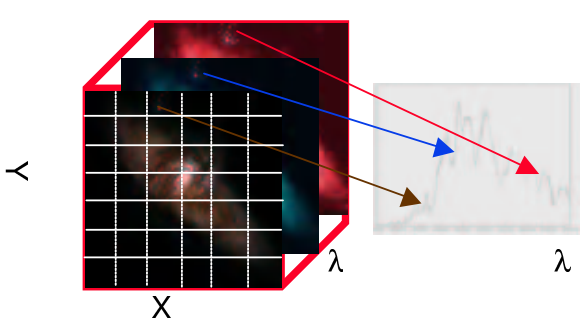

Fig. 20.— The principal of 3D spectroscopy where a spectrum is taken for each spatial position.

technique, developed since 1938 in order to minimize slit losses, is very powerful (Bowen 1938). The new generation of image slicers improves the efficiency and the compactness of the system and appears to be a very well adapted solution for the SNAP mission.

Figure 22 shows the principle of this technique. The field of view is sliced along N (in the drawing $N = 3$, for SNAP $N = 20$) strips on a slicing mirror, consisting of a stack of N plates where the active surface is on an edge. Each of the N slices re-images the telescope pupil, creating N telescope pupil images in the pupil plane. Thanks to a tilt adapted to each individual slice, the N pupil images lie along a line. In the pupil plane, a line of "pupil mirrors" is arranged. Each pupil mirror is placed on a pupil image and reimages the field strip. These images are arranged along a line and form a "pseudo-slit". At this stage, therefore, we have an image of each of the N strips of the field of view. The pseudo-slit is placed in the entrance plane of the spectrograph, acting as the entrance slit.

A last line of mirrors is placed on the pseudo-slit. This line adapts the output pupil of the slicer into the input pupil of the spectrograph.

4.5.2. *Instrument Concept*

The spectrograph components are summarized in the block diagram shown in Figure 23 with the principal components described below.

Relay Optics

This unit is the interface between the telescope beam and the instrument. Some telescope aberrations can be corrected within this optical system. A simple three-mirror configuration should be sufficient to allow picking off the beam at a point most convenient for the spectrometer.

Slicer Unit

The slicer unit acts as a field reformatting system. As described above, the principle is to slice a 2D field of view into long strips and optically align all the strips to form a long spectrograph entrance slit. The slicing mirror is comprised of a stack of slicers. Each slicer has an optically active spherical surface on one edge. A line of pupil mirrors does the reformatting. Each pupil mirror sends the beam to a slit mirror, which adapts the pupil to the entrance of the spectrograph.

TABLE 7

SPECTROGRAPH SPECIFICATIONS

Property	Visible	NIR
Wavelength coverage (μm)	0.35-0.98	0.98-1.70
Field of view	3.0" $\times$ 3.0"	3.0" $\times$ 3.0"
Spatial resolution element (arcsec)	0.15	0.15
Number of slices	20	20
Spectral resolution, $\lambda/\delta\lambda$	100	100

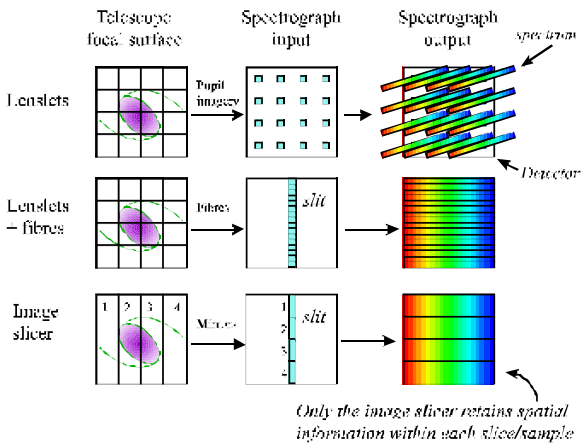

Fig. 21.— Three generic techniques for Integral Field Spectroscopy; using lenslets, lenslets and fibers, and an imager slicer. The image slicer is preferred by SNAP as it allows unconstrained placement of the dispersed spectra on the detector and has high throughput (courtesy J. Allington-Smith, Durham U.).

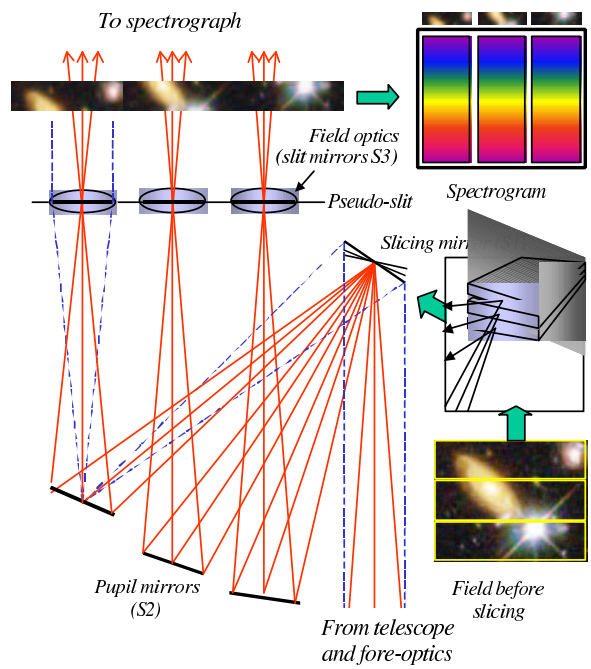

Fig. 22.— Principle of the image slicer. The field of view is sliced along N (here $N = 3$) strips on a slicing mirror. Each slice re-images the telescope pupil onto a line of "pupil mirrors" which reimages the field strip along a "pseudo-slit". The pseudo-slit is placed in the entrance plane of the spectrograph, acting as the entrance slit (courtesy J. Allington-Smith, Durham U.).

The long thin active surface of each individual slicer will produce a large diffraction effect. In order to minimize flux losses to a few percent, the spectrograph entrance pupil must be oversized. A combined theoretical and experimental approach is underway at Laboratoire d'Astrophysique de Marseille to define the optimum entrance pupil for a JWST application (in the infrared bands 1-5 μm). This will be directly adapted for the SNAP concept.

The baseline requirements on the slicer unit are an accuracy of $\leq \lambda/10$ RMS on the optical surfaces and a surface roughness of ≤ 5 nm RMS. Existing prototypes fully meet these specifications.

Optical Bench

Thanks to the moderate beam aperture and field of view, the spectrograph optics will be straightforward. The baseline is a classical dichroic spectrograph: one collimator mirror, one prism with a dichroic crystal, and two camera mirrors are required. Using spherical shapes for all the mirrors would provide an adequately sharp image, but using aspheric mirrors will make it possible to have a very compact spectrograph. The prism solution is well matched to the requirement of a flat resolution over the whole wavelength range. The dichroic crystal allows covering two channels simultaneously: one for the visible (e.g.. 0.35–0.98 μm) and one for the infrared (0.98–1.70 μm).

Detectors

In the visible, the main goals are high quantum efficiency and very low noise. Given concerns over degradation due to radiation exposure and the poor performance of conventional thinned CCD's in the red part of the visible, we anticipate using the LBNL CCD's. Thinned, back-side illuminated, low-noise conventional CCD's of 1024 $\times$ 1024 pixels are an alternative option. In the NIR, some factors constrain the detector technologies. The operating temperature will be dictated by the detector dark current. HgCdTe arrays with cutoff wavelength of 1.7 μm are currently under consideration which allow operation in the 130-140 K range. A detailed list of the performance specifications for the detectors is provided in Table 8. To achieve the listed performance in read noise and dark current, a multiple sampling technique is required. To optimize exposure time, the impact of the rate of cosmic rays on the readout noise is under study.

4.5.3. Efficiency Estimate

Simulations of the efficiency of the instrument show a cumulative efficiency of the instrument from the relay optic to the detector at a level better than 50% in the visible and than 40% in the infrared. This excellent performance is due to high slicer efficiency and is based on a conservative value for the efficiency of individual mirrors (98%), much lower than is expected from a silver coating at these wavelengths. The principal losses are from the prism (also conservatively estimated at 80%), and from the detector. Figure 24 shows the full response of the instrument for different detectors (LBL CCD's, HgCdTe with JWST specification, thinned HgCdTe with 60% efficiency across the band, and WFC3 HgCdTe specs).

4.6. Telemetry

The observation time of SNAP is partitioned roughly 60% to photometry and 40% to targeted spectroscopy with photometry. The former is divided into a sequence of 300s exposures followed by 30s of sensor readout. The latter is comprised of exposures varying from a few seconds to a thousand seconds. For the longer exposure times, the spectrograph NIR detector is continuously read in up-the-ramp mode. Imaging is possible during spectroscopic exposures; the imager is read as in photometry mode except that the exposure times vary, determined by the time to achieve a required S/N in the spectrograph for a particular SN. For each imaging exposure, the CCD devices produce a single frame of correlated double sampled data while the NIR devices produce two frames (each containing the average of multiple reads), one for post reset values and the other for post integration values so that the digital correlated double sampling can be done on the ground. In the above scenario, photometry generates 5.4 Tb per orbit and spectroscopy generates 1 Tb per orbit.

The operating concept for processing the raw data is to perform only lossless compression of the frames in the satellite. We assume that a factor of two is easily done; a greater compression factor is probably achievable. The primary motivations are to be able to look retrospectively into the data to better determine a SN explosion time and to be able to co-add many months of data for weak lensing science to extract weak signals from the per frame noise. With this approach we avoid developing flight software for automated acquisition and processing of reference, dark and flat frames

TABLE 8
SPECTROGRAPH DETECTOR SPECIFICATIONS

	Visible	NIR
Detector size	1k × 1k	1k × 1k
Pixel size (μm)	10-20	18-20
Detector temperature(K)	140	130-140
$\langle$QE$\rangle$(%)	>80	>60
Read noise(e^-)	2	5
Dark current(e^-/pixel/s)	0.001	0.02

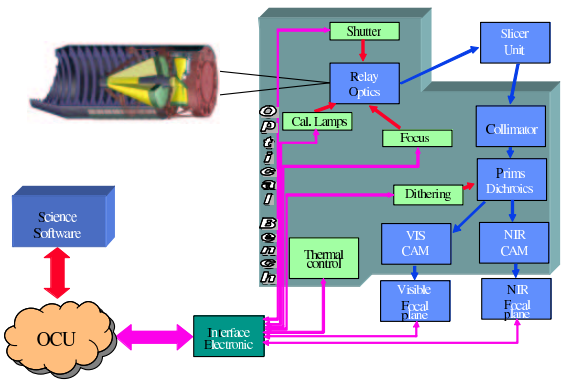

Fig. 23.— Spectroscope block diagram.

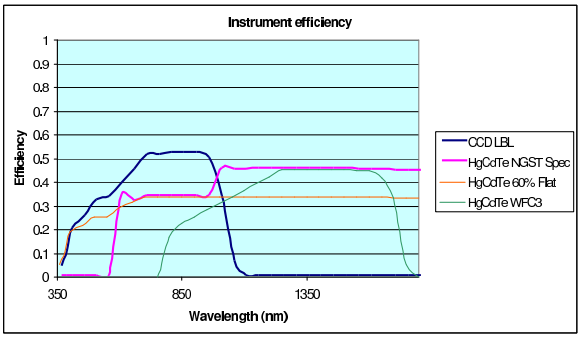

Fig. 24.— Efficiency of the spectrograph given different detectors.

and applying them irrecoverably to data frames. The consequence is that SNAP will require about 400 Gb of flight data storage.

During each 72-hour orbit, 12 hours are spent within or beneath the geomagnetically trapped electron belts and are unsuitable for astronomy. Of this, there will be at least a 6 hour contact time with the 11-m dish at the ground station located at the University of California Berkeley Space Sciences Laboratory. To be able to safely downlink the 400 GB of stored data will require a telemetry bandwidth of 300 Mbs modulated onto a Ka-band carrier.

5. SNAP Supernova Cosmology Simulation

We have developed a detailed parametrized simulator of supernova cosmology missions. The simulation package and results from it are described in Akerlof et al. (2003). We describe here its use in projecting the scientific yield from the SNAP supernova mission.

For the telescope/camera configuration and observing plan described in the previous sections, we generate a list of Type Ia supernovae and their associated host galaxies in the observed field of view during the course of the survey. The incident flux at the telescope is calculated for each supernova, accounting for the underlying cosmology, magnification from gravitational lensing, and host and Galactic dust. The photometric observations of the supernovae from the SNAP scanning strategy are simulated, resulting in multi-band light curves for each event.

These rest-frame B and V light curves are fit to SN Ia-class templates while the light curves in other filters are fit to a polynomial, in order to measure the magnitude, color, and light-curve parameters of each

supernova. Triggered spectroscopic observations are simulated through Fisher-matrix techniques (Bernstein & Kim 2003) which predict the quality of the spectroscopic parameter measurements. The supernova's light-curve and spectral parameters are then used to determine its distance modulus, along with host-galaxy extinction (A_V and R_V of the Cardelli, Clayton, & Mathis (1989) dust model) and its individual absolute magnitude.

Given the SNAP supernova distribution and expected distance moduli, folded with the expected supernovae from the Nearby Supernova Factory, we fit the cosmological parameters. While this can be done generally, most often we concentrate on the dark-energy parameters w_0 and w' assuming a flat universe, a fiducial cosmological constant dark energy, and a prior 0.03 uncertainty in Ω_M. A linearly increasing irreducible magnitude systematic of $\sigma_m = 0.02(z/1.7)$ in a 0.1 redshift bin is also included. Marginalizing for each parameter, we get uncertainties in w_0 of 0.06 and w' of ~ 0.25. Note that the differences between these errors and the ones shown in Table 1, reflect both the different Ω_M prior and the extremely high signal-to-noise that we will obtain for our low to mid-redshift supernovae.

To explore how SNAP will be able to distinguish between different dark-energy models, we fit w_0 and w' choosing as fiducials several postulated theories that account for an accelerating Universe; a cosmological constant, a supergravity model, vacuum metamorphosis, axion dark energy, and a leaping kinetic model. The 68% confidence contours are given for SNAP supernovae, and for SNAP supernovae used in conjunction with the data anticipated from the Planck mission. We marginalize over the absolute magnitude and Ω_M. In the case of SNAP + Planck we do not impose a prior on Ω_M. Note that we have not included the contribution of SNAP weak-lensing data which will add important complementary constraints.

Even with just SNAP supernovae, the chosen models are distinct, with the fiducial values indicated by the x's lying outside the 68% contours of other models. Additionally, CMB information restricts the allowed parameter space even more. SNAP and complementary data will give important guidance to the true nature of dark energy.

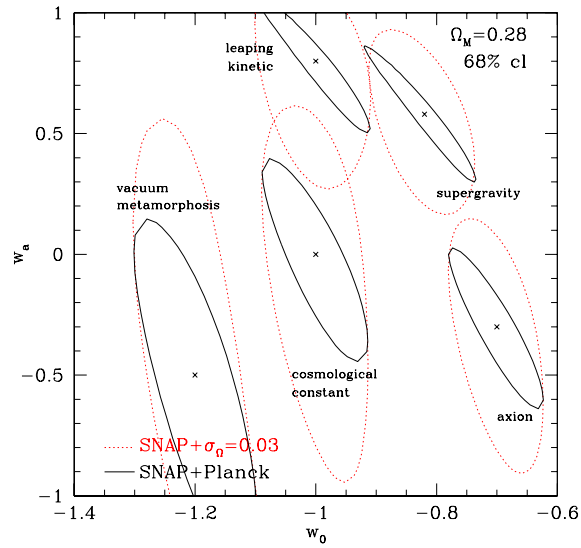

Fig. 25.— The confidence region in the dark-energy parameters for different fiducial dark-energy models representing very different physical origins: a cosmological constant, a supergravity model, vacuum metamorphosis, axion dark energy, and a leaping kinetic model. In red are the results from SNAP and in black with SNAP and Planck. Note that $w' \approx w_a/2$.

6. Ancillary Science with the SNAP Survey Fields

The SNAP surveys will have an unprecedented combination of depth, solid-angle, angular resolution, temporal sampling, and wavelength coverage from the optical to the NIR. We explore the properties of the surveys and their potential scientific yield.

6.1. SNAP Survey Depth

Based on the telescope and camera characteristics, we quantify the expected depth, solid-angle, and time resolution of the SNAP supernova and weak lensing surveys. The telescope and camera properties of SNAP have been modeled and incorporated into an advanced exposure-time calculator (ETC) (Bernstein 2002). Besides having all the bells and whistles of a standard ETC, our ETC includes unique handling of the pixel response function, undersampling, dithering, and probabilistic cosmic-ray rejection. As mentioned in §4.3, SNAP will rely on dithering to recover spatial resolution from its undersampled pixels.

The high cosmic-ray flux produces a non-trivial re-

duction of effective exposure times; pixels from a single exposure that are contaminated by a cosmic ray are assumed to be recognized through median filtering and dropped in the dithered reconstruction. Short individual exposure times limit the contamination: 300 second exposures give a 68% probability that there will be no cosmic-ray contamination at a given position on any of the four dithers that make up a pointing.

The magnitude depths for individual scans and co-added images of the SNAP supernova fields are calculated for each filter. The limiting magnitude for any given point is probabilistic, due to the random occurrence of cosmic rays. Table 9 shows the 50th-percentile limiting AB magnitude for a $S/N = 5$ point source for each filter in the surveys.

The SNAP observing strategy provides remarkably even depth over the range of filters. For a given filter, individual scans of the supernova and lensing surveys are only ~ 0.75 magnitudes shallower than the Hubble Deep Fields (HDFs) while the SN fields co-added over time are ~ 1.5 magnitudes deeper than the HDFs (Williams et al. 1996). SNAP has the additional advantage of having nine filters observing to this depth, compared to the four filters of the HDFs, and 9000 times the area in the deep supernova survey; when these data from all filters are combined, the limiting magnitude increases by 0.6 magnitudes.

SNAP fields will contain many faint diffuse galaxies whose detection is important for the weak-lensing survey, and for other potential science projects. The limiting magnitudes for Gaussian-aperture photometry of an exponential-disk galaxy with FWHM=0.12" are shown in Table 10.

6.2. Ancillary Science

In this section we give a brief discussion of possible science that can be obtained from the SNAP surveys. This list is by no means complete in its breadth nor depth.

The Sloan Digital Sky Survey(SDSS) (D. G. York *et al.* 2000) and HDFs (Williams et al. 1996; R. E. Williams *et al.* 2000) have demonstrated the vast range of science that can be obtained from wide and deep multi-band surveys. SNAP will produce surveys that dwarf the 0.0016 square degrees size of the HDFs and go even deeper, with time-sampling for its supernova fields. The SNAP lensing field is about the same size as the Sloan Southern Survey and CFHT Legacy Survey fields but several magnitudes fainter and deeper in redshift. This combination of depth, temporal coverage, filter coverage over a broad wavelength range, diffraction-limited seeing, and wide field make SNAP imaging surveys uniquely powerful in the study of a wide range of objects and phenomena:

- Galaxies — Within the 15 square degree supernova survey area, SNAP will make accurate photometric redshift measurements for at least 10^7 galaxies from redshift 0 to 3.5, through more than 90% of the age of the universe. Statistical studies are possible with such a large sample, e.g. the determination of the galaxy luminosity function and color distributions as a function of redshift. Photometric redshifts can be estimated from the 4000 Å break for galaxies out to about $z = 3.2$. For galaxies at still higher redshift, the simplest indicator is the Lyman break. For SNAP, the Lyman break enters the optical imager around redshift 3. In principle it can be followed using SNAP data beyond redshift 10, allowing identification of extremely high redshift galaxies. The magnitude depth also allows discovery of low-surface-brightness and very high-redshift galaxies. High-resolution images will provide a view of the internal structure of galaxies and their interactions with each other. This data set, which will include morphological information for every object, will provide a unique opportunity to study the evolution of galaxies. The flood of galaxy evolution papers based on the Hubble Deep Fields only hints at what will be possible with the SNAP imaging data set.

- Galaxy clusters — Galaxy clusters, the most massive bound objects in the universe, provide important probes of our understanding of structure formation. Constraining their formation and evolution is an important observational goal for the coming decade. Recent advances have overcome earlier limitations of optically selected cluster samples, essentially by using photometric redshift information to eliminate projection effects. The SNAP surveys will provide detailed information on roughly 15,000 galaxy clusters with masses above 5×10^{13} $M_\odot$. The epoch of galaxy-cluster formation is tightly linked with the mass density of the Universe, Ω_M, providing an independent cosmological measurement complementary to SNAP's

TABLE 9

THE SNAP 50TH-PERCENTILE AB MAGNITUDE SURVEY DEPTH FOR A POINT SOURCE $S/N = 5$.[a]

Filter	λ_{eff}(Å)	$\Delta\lambda$(Å)	SN Survey (AB mag)		Lensing Survey (AB mag)
			Scan	Co-added Scans	
1	4400	1000	27.9	30.6	28.3
2	5060	1150	27.8	30.5	28.2
3	5819	1323	27.8	30.4	28.1
4	6692	1521	27.7	30.4	28.1
5	7696	1749	27.7	30.3	28.0
6	8850	2011	27.5	30.2	27.9
7	10178	2313	27.5	30.2	27.8
8	11704	2660	27.4	30.1	27.8
9	13460	3059	27.4	30.0	27.7

[a]Random cosmic-ray hits make the S/N for a given position probabilistic. The choice of filter set is currently subject to optimization studies; the filters and depths presented here are meant to be illustrative.

TABLE 10

THE SNAP AB MAGNITUDE SURVEY DEPTH FOR AN EXPONENTIAL-DISK GALAXY WITH FWHM=0.12" WITH $S/N = 10$.[a]

Filter	λ_{eff}(Å)	$\Delta\lambda$(Å)	SN Survey (AB mag)		Lensing Survey (AB mag)
			Scan	Co-added Scans	
1	4400	1000	26.4	29.1	26.8
2	5060	1150	26.3	29.0	26.7
3	5819	1323	26.3	29.0	26.6
4	6692	1521	26.2	28.9	26.6
5	7696	1749	26.3	28.9	26.6
6	8850	2011	26.2	28.8	26.5
7	10178	2313	26.3	28.9	26.6
8	11704	2660	26.2	28.9	26.6
9	13460	3059	26.2	28.9	26.5

[a]The choice of filter set is currently subject to optimization studies; the filters and depths presented here are meant to be illustrative.

primary missions.

- Quasars — The NIR photometry extends the redshift range for quasar discovery ($6.3 < z < 12$) using colors and dropout surveys. Discoveries will also move much fainter into the quasar luminosity function. Quasars are identified in multi-color imaging surveys by their non-stellar colors. This method has been shown by the Sloan Digital Sky Survey to be extremely effective at identifying quasars to redshift 6 and beyond. SDSS quasar discovery is limited to redshift 6 by the CCD sensitivity cutoff at 1.0 μm (Pentericci et al. 2002) (see Fig. 26). The most distant SDSS quasar, at redshift 6.28, has a z-band magnitude of 20. By probing to wavelengths 1.7 times greater, and to depths 9 magnitudes fainter, SNAP will be able to detect quasars beyond redshift 10, and to probe the quasar luminosity function to 100 times fainter than the brightest quasars. SNAP's ability to identify diffuse objects associated with quasars may present many opportunities for the study of galaxy formation.

- Gamma-ray burst afterglows — Current evidence suggests that gamma-ray bursts are associated with the collapse of massive stars which live short lives and die where they are born. As a result, GRB's may trace the cosmic star formation rate. If so, there should be GRB's essentially coincident with the epoch of formation of the first stars. The most distant GRB known occurred at redshift of 3.4. SNAP will be able to identify GRB afterglows, and the orphan afterglows predicted by some models of beaming in GRB's to $z = 10$. Such orphan afterglows may even be detected as backgrounds to the SNe search.

- Reionization history — The universe became neutral at the time of recombination, around $z = 1000$, and the thermal radiation from that epoch travels to us undisturbed as the cosmic microwave background radiation. The lack of a Gunn-Peterson effect in the spectra of most quasars demonstrates that the universe was reionized at some time between $z = 1000$ and $z = 6$. The source of the ionizing radiation is the subject of substantial speculation. The recent discovery of an apparent Gunn-Peterson trough in the most distant $z > 6$ SDSS quasar spectra may provide the first glimpse of the epoch of reionization. By identifying many quasars and galaxies to $z = 10$, SNAP will set the stage for mapping the epoch of reionization in unprecedented detail. In combination with ground based and JWST spectroscopy, it will enable measurements of the proximity effect and studies of the spatial structure of reionization.

- Transients/Variables — The discovery and observation of SNe Ia are the primary goals of SNAP, but transient "backgrounds" are interesting in their own right: quasars, active-galactic-nuclei, gamma-ray-burst optical counterparts, supernovae of other types, variable stars, and eclipsing binaries. Of particular interest to cosmology is time-delay studies with the expected large number of strongly lensed variables. Gravitational microlensing surveys of stars and quasars to measure dark matter are also possible.

- Stars — Faint limiting magnitudes and excellent star-galaxy separation will yield faint dwarf and halo stars. Proper motion can be detected with high-resolution and a long time baseline. SNAP's accurate colors will yield excellent photometric parallaxes to all stars in the field. The geometry and substructure of the Galactic halo and disk in the direction of the SNAP fields can be mapped. Of particular interest would be a census of low-mass L and T stars and brown dwarfs throughout the Milky Way disk (Leggett et al. 2000) (see Fig. 27).

- Solar-system objects — The peculiar motion in the time-series data will facilitate the identification of local objects such as asteroids and Kuiper-belt objects. SNAP time series data will provide an excellent probe of faint, red objects in the Kuiper belt and beyond. A 2-3 month SNAP survey would detect 10–50,000 Kuiper belt objects down to the size of the Comet Halley's nucleus.

- Gravitational lensing — The high spatial resolution of SNAP NIR observations will enable the discovery of a large number of new strong lenses. The NIR observations, which are much less sensitive to dust extinction within the lens galaxy, are especially important in this regard.

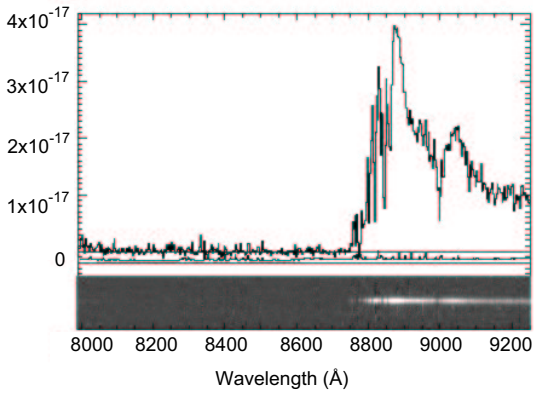

Fig. 26.— This figure, from Pentericci et al. (2002), shows a VLT/FORS2 spectrum of the $z = 6.28$ quasar SDSS J1030+0524 in the observed frame. The bottom panel shows a gray-scale representation of the sky-subtracted two-dimensional spectrum plotted on the same wavelength scale. Note the apparent Gunn-Peterson trough: a complete absence of flux from 8450 to 8710 Å.

The output from the SDSS has demonstrated how the natural byproducts of a wide-field survey can produce scientific yield well beyond the scope of its primary purpose. Individual objects found on SDSS images are routinely observed spectroscopically at the largest telescopes in the world, fulfilling the historical trend of small-aperture telescope imaging feeding targets for large-aperture telescope spectroscopy. The SNAP surveys will provide a similar opportunity in working with JWST and the next generation of ground-based wide-aperture telescopes.

7. Conclusion

The discoveries of recent years make this a fascinating new era of empirical cosmology, capable of addressing fundamental questions. The continued use of supernovae to provide precision measurements of dark-energy properties requires a new stringent dataset in order to control systematic and statistical errors; large numbers of supernovae over an extended redshift range with light curves and spectra measured to high signal-to-noise.

Based on these data requirements, we have developed the Supernova / Acceleration Probe, consisting of a detailed observing program carried out with an optimized wide-field telescope and attendant imaging

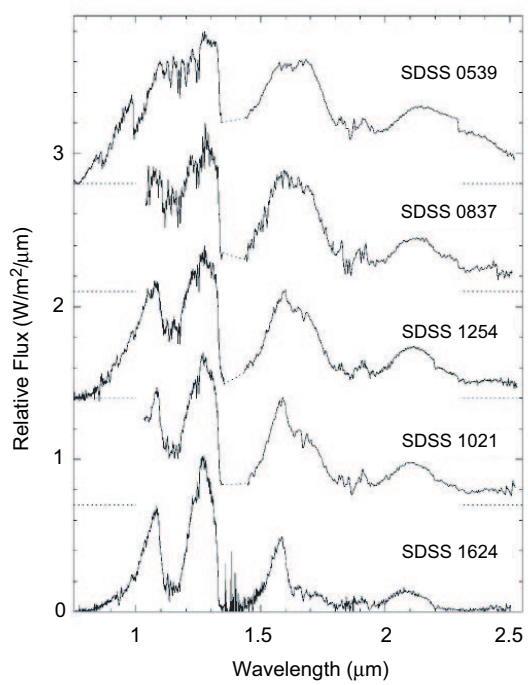

Fig. 27.— This figure, from Leggett et al. (2000), shows optical/NIR spectra for five stars ranging from a late L dwarf at the top through a series of T dwarfs. The nearly complete absence of optical flux from these very cool stars, along with their strong NIR emission, is apparent.

and spectrograph instruments. The optical, mechanical, and thermal studies and analysis conducted to date indicate that this telescope is manufacturable and testable using proven techniques. The imager will provide efficient multiplexed supernova discovery and light-curve building while the spectrograph satisfies the performance requirements for measuring key spectral features of the faintest supernovae.

The baseline design presented in this paper addresses the many requirements necessary for a high-precision supernova experiment. We are currently engaged in a conceptual design study for SNAP, using numerical simulations and trade studies to refine the mission concept and quantify the expected science yield of SNAP. This paper will be followed up with further results of these studies and the progress in the optimization of SNAP.

SNAP provides a combination of depth, solid-angle, angular resolution, and PSF stability well beyond what has heretofore been achieved. These properties naturally lend themselves toward a weak gravitational lensing survey, the second SNAP primary science mission. This independent experimental approach complements the cosmological parameter measurements from supernovae.

SNAP presents a unique opportunity to probe the dark energy and advance our understanding of the Universe. The principal survey missions of SNAP will also produce a cornucopia of observations capable of revolutionizing other areas of astrophysics and cosmology. And beyond this science, additional studies will be produced from data taken after completion of the SNAP primary missions; a guest survey program is envisioned filling the remaining satellite lifetime to allow the full potential of SNAP to be realized.

Acknowledgments

This work was supported by the Director, Office of Science, of the U.S. Department of Energy under Contract No. DE-AC03-76SF00098.

REFERENCES

Aguirre, A. N. 1999, ApJ, 512, L19

Akerlof, C., et al. 2003, in preparation

Aldering, G., et al. 2003. An Overview of the Nearby Supernova Factory. In Proc. SPIE, volume 4836

Aldering, G., Knop, R., & Nugent, P. 2000, AJ, 119, 2110–2117

Bahcall, N. A., Ostriker, J. P., Perlmutter, S., & Steinhardt, P. J. 1999, Science, 284, 1481

Balbi, A., Ade, P., Bock, J., Borrill, J., Boscaleri, A., De Bernardis, P., Ferreira, P. G., Hanany, S., Hristov, V., Jaffe, A. H., Lee, A. T., Oh, S., Pascale, E., Rabii, B., Richards, P. L., Smoot, G. F., Stompor, R., Winant, C. D., & Wu, J. H. P. 2000, Astrophys. J., 545, L1–LL4

Bebek, C., et al. 2003. SNAP Focal Plane. In Proc. SPIE Vol. 4854, Astronomical Telescopes and Instrumentation, volume 4854

Bernstein, G. 2002, PASP, 114, 98–111

Bernstein, G., & Kim, A. 2003, in preparation

Borys, C., Chapman, S. C., Halpern, M., & Scott, D. 2002, MNRAS, 330, L63–L67

Bowen, I. S. 1938, ApJ, 88, 113–+

Branch, D., & van den Bergh, S. 1993, AJ, 105, 2231

Caldwell, R. R., Dave, R., & Steinhardt, P. J. 1998, Physical Review Letters, 80, 1582–1585

Cardelli, J. A., Clayton, G. C., & Mathis, J. S. 1989, ApJ, 345, 245

Coble, K., Dodelson, S., & Frieman, J. A. 1997, Phys. Rev. D, 55, 1851–1859

D. G. York *et al.* 2000, AJ, 120, 1579–1587

Efstathiou, G., Moody, S., Peacock, J. A., Percival, W. J., Baugh, C., Bland-Hawthorn, J., Bridges, T., Cannon, R., Cole, S., Colless, M., Collins, C., Couch, W., Dalton, G., de Propris, R., Driver, S. P., Ellis, R. S., Frenk, C. S., Glazebrook, K., Jackson, C., Lahav, O., Lewis, I., Lumsden, S., Maddox, S., Norberg, P., Peterson, B. A., Sutherland, W., & Taylor, K. 2002, MNRAS, 330, L29–L35

Frieman, J. A., Hill, C. T., Stebbins, A., & Waga, I. 1995, Phys. Rev. Lett., 75, 2077–2080

Garnavich, P. M., Jha, S., Challis, P., Clocchiatti, A., Diercks, A., Filippenko, A. V., Gilliland, R. L., Hogan, C. J., Kirshner, R. P., Leibundgut, B., Phillips, M. M., Reiss, D., Riess, A. G., Schmidt, B. P., Schommer, R. A., Smith, R. C., Spyromilio,

J., Stubbs, C., Suntzeff, N. B., Tonry, J., & Carroll, S. M. 1998, ApJ, 509, 74–79

Groom, D. E., Holland, S. E., Levi, M. E., Palaio, N. P., Perlmutter, S., Stover, R. J., & Wei, M. 2000, Nuclear Instruments and Methods in Physics Research A, 442, 216–222

Hamuy, M., Phillips, M. M., Suntzeff, N. B., Schommer, R. A., Maza, J., & Aviles, R. 1996, Astron. J., 112, 2391

Hamuy, M., Trager, S. C., Pinto, P. A., Phillips, M. M., Schommer, R. A., Ivanov, V., & Suntzeff, N. B. 2000, Astron. J., 120, 1479–1486

Höflich, P., Wheeler, J. C., & Thielemann, F. K. 1998, Astrophys. J., 495, 617

Holland, S. E., Wei, M., Ji, K., Brown, W. E., Gilmore, D. K., Stover, R. J., Groom, D. E., Levi, M. E., Palaio, N., & Perlmutter, S. 1999. Large Format CCD Image Sensors Fabricated on High Resistivity Silicon. In IEEE Workshop on Charge-Coupled Devices and Advanced Image Sensors, page 239

Kim, A., Linder, E., Miquel, R., & Mostek, N. 2003, in preparation

Korsch, D. 1977, ApOpt, 16, 2074

Lampton, M. *et al.*. 2002. SNAP Telescope. In Survey and Other Telescope Technologies and Discoveries, volume 4849 of *Proceedings of SPIE*

Lange, A. E., Ade, P. A., Bock, J. J., Bond, J. R., Borrill, J., Boscaleri, A., Coble, K., Crill, B. P., de Bernardis, P., Farese, P., Ferreira, P., Ganga, K., Giacometti, M., Hivon, E., Hristov, V. V., Iacoangeli, A., Jaffe, A. H., Martinis, L., Masi, S., Mauskopf, P. D., Melchiorri, A., Montroy, T., Netterfield, C. B., Pascale, E., Piacentini, F., Pogosyan, D., Prunet, S., Rao, S., Romeo, G., Ruhl, J. E., Scaramuzzi, F., & Sforna, D. 2001, Phys. Rev. D, 63, 42001

Leggett, S. K., Geballe, T. R., Fan, X., Schneider, D. P., Gunn, J. E., Lupton, R. H., Knapp, G. R., Strauss, M. A., McDaniel, A., Golimowski, D. A., Henry, T. J., Peng, E., Tsvetanov, Z. I., Uomoto, A., Zheng, W., Hill, G. J., Ramsey, L. W., Anderson, S. F., Annis, J. A., Bahcall, N. A., Brinkmann, J., Chen, B., Csabai, I., Fukugita, M., Hennessy, G. S., Hindsley, R. B., Ivezić, Ž., Lamb, D. Q., Munn, J. A., Pier, J. R., Schlegel, D. J., Smith, J. A., Stoughton, C., Thakar, A. R., & York, D. G. 2000, ApJ, 536, L35–L38

Lentz, E. J., Baron, E., Branch, D., Hauschildt, P. H., & Nugent, P. E. 2000, ApJ, 530, 966–976

Linder, E. V., & Huterer, D. 2002. Importance of Supernovae at z $>$ 1.5 to Probe Dark Energy. In eprint arXiv:astro-ph/0208138, pages 8138–+

Massey, R., et al. 2003, in preparation

Nugent, P., Phillips, M., Baron, E., Branch, D., & Hauschildt, P. 1995, Astrophys. J., 455, L147

Paerels, F., Petric, A., Telis, G., & Helfand, D. J. 2002, American Astronomical Society Meeting, 201, 0–+

Pentericci, L., Fan, X., Rix, H., Strauss, M. A., Narayanan, V. K., Richards, G. T., Schneider, D. P., Krolik, J., Heckman, T., Brinkmann, J., Lamb, D. Q., & Szokoly, G. P. 2002, AJ, 123, 2151–2158

Percival, W. J., Sutherland, W., Peacock, J. A., Baugh, C. M., Bland-Hawthorn, J., Bridges, T., Cannon, R., Cole, S., Colless, M., Collins, C., Couch, W., Dalton, G., De Propris, R., Driver, S. P., Efstathiou, G., Ellis, R. S., Frenk, C. S., Glazebrook, K., Jackson, C., Lahav, O., Lewis, I., Lumsden, S., Maddox, S., Moody, S., Norberg, P., Peterson, B. A., & Taylor, K. 2002, MNRAS, 337, 1068–1080

Perlmutter, S., Turner, M. S., & White, M. 1999, Phys. Rev. Lett., 83, 670–673

Perlmutter, S., Aldering, G., Goldhaber, G., Knop, R. A., Nugent, P., Castro, P. G., Deustua, S., Fabbro, S., Goobar, A., Groom, D. E., Hook, I. M., Kim, A. G., Kim, M. Y., Lee, J. C., Nunes, N. J., Pain, R., Pennypacker, C. R., Quimby, R., Lidman, C., Ellis, R. S., Irwin, M., McMahon, R. G., Ruiz-Lapuente, P., Walton, N., Schaefer, B., Boyle, B. J., Filippenko, A. V., Matheson, T., Fruchter, A. S., Panagia, N., Newberg, H. J. M., Couch, W. J., & The Supernova Cosmology Project 1999, ApJ, 517, 565–586

R. E. Williams *et al.* 2000, AJ, 120, 2735–2746

Ratra, B., & Peebles, P. J. E. 1988, Phys. Rev. D, 37, 3406–3427

Refregier, A. 2003, ARAA, in press

Refregier, A., et al. 2003, in preparation

Rhodes, J., et al. 2003, in preparation

Rhodes, J., Refregier, A., & Groth, E. J. 2000, ApJ, 536, 79–100

Riess, A. G., Filippenko, A. V., Challis, P., Clocchiatti, A., Diercks, A., Garnavich, P. M., Gilliland, R. L., Hogan, C. J., Jha, S., Kirshner, R. P., Leibundgut, B., Phillips, M. M., Reiss, D., Schmidt, B. P., Schommer, R. A., Smith, R. C., Spyromilio, J., Stubbs, C., Suntzeff, N. B., & Tonry, J. 1998, AJ, 116, 1009–1038

Scott, S. E., Fox, M. J., Dunlop, J. S., Serjeant, S., Peacock, J. A., Ivison, R. J., Oliver, S., Mann, R. G., Lawrence, A., Efstathiou, A., Rowan-Robinson, M., Hughes, D. H., Archibald, E. N., Blain, A., & Longair, M. 2002, MNRAS, 331, 817–838

Spergel, D. L., et al. 2003, ApJ, submitted

Stover, R. J., Wei, M., Ji, K., Brown, W. E., Gilmore, D. K., Holland, S. E., Groom, D. E., Levi, M. E., Palaio, N., & Perlmutter, S. 2000. A 2Kx2K high resistivity CCD. In Optical Detectors for Astronomy II: State-of-the-Art at the Turn of the Millenium, page 239

Sullivan, M., Ellis, R. S., Aldering, G., Amanullah, R., Astier, P., Blanc, G., Burns, M. S., Conley, A., Deustua, S. E., Doi, M., Fabbro, S., Folatelli, G., Fruchter, A. S., Garavini, G., Gibbons, R., Goldhaber, G., Goobar, A., Groom, D. E., Hardin, D., Hook, I., Howell, D. A., Irwin, M., Kim, A. G., Knop, R. A., Lidman, C., McMahon, R., Mendez, J., Nobili, S., Nugent, P. E., Pain, R., Panagia, N., Pennypacker, C. R., Perlmutter, S., Quimby, R., Raux, J., Regnault, N., Ruiz-Lapuente, P., Schaefer, B., Schahmaneche, K., Spadafora, A. L., Walton, N. A., Wang, L., Wood-Vasey, W. M., & Yasuda, N. 2002. The Hubble Diagram of Type Ia Supernovae as a Function of Host Galaxy Morphology. In eprint arXiv:astro-ph/0211444, pages 11444–+

Taylor, A. N. 2001, ArXiv Astrophysics e-prints, pages 0111605–+

Turner, M. S., & White, M. 1997, Phys. Rev. D, 56, 4439–

Vilenkin, A. 1984, Physical Review Letters, 53, 1016–1018

Vilenkin, A., & Shellard, E. 1994. Cosmic Strings and other Topological Defects, Cambridge, U.K.: Cambridge University Press

Weller, J., & Albrecht, A. 2001, Phys. Rev. Lett., 86, 1939–1942

Weller, J., & Albrecht, A. 2002, Phys. Rev. D, 65, 3512

Williams, R. E., et al. 1996, AJ, 112, 1335

Zlatev, I., Wang, L., & Steinhardt, P. J. 1999, Physical Review Letters, 82, 896–899

This 2-column preprint was prepared with the AAS LaTeX macros v5.0.